Design and Analysis of a PVDF Acoustic Transducer Towards an Imager for Mobile Underwater Sensor Networks

Benjamin T Eovino

Electrical Engineering and Computer Sciences
University of California at Berkeley

Technical Report No. UCB/EECS-2015-154
http://www.eecs.berkeley.edu/Pubs/TechRpts/2015/EECS-2015-154.html

May 26, 2015

Design and Analysis of a PVDF Acoustic Transducer Towards an Imager for Mobile Underwater Sensor Networks

by

Benjamin Eric Eovino

BS (University of California, Santa Barbara) 2013

A report submitted in partial satisfaction of the

requirements for the degree of

Masters of Science, Plan II

in

Electrical Engineering and Computer Science

at the

University of California at Berkeley

Committee in Charge:

Professor Albert P. Pisano, Chair

Professor Liwei Lin

Spring 2015

Design and Analysis of a PVDF Acoustic Transducer Towards an Imager for Mobile Underwater Sensor Networks

by

Benjamin Eric Eovino

Abstract

Design and Analysis of a PVDF Acoustic Transducer Towards an Imager for Mobile Underwater Sensor Networks

by

Benjamin Eric Eovino

Masters of Science, Plan II in Electrical Engineering and Computer Science

University of California, Berkeley

Professor Albert P. Pisano, Chair

The ocean is home to many exotic ecosystems, a substantial source of the world's total crude oil, susceptible to military infiltration, and yet still massively undersampled and underexplored. Recently, mobile underwater sensor networks have been gaining traction as a method for monitoring our oceans with better spatial and temporal resolution. In this application, the most viable way of imaging the environment is by using acoustics. This is precluded, however, by a current lack of suitable acoustic transducers.

In this report, a Polyvinylidene Fluoride-based acoustic transducer for use in underwater wireless sensor networks is proposed and evaluated. It is suggested as a small, low-cost device that is robust to hydrostatic pressures. Furthermore, its ability to act as both an active and passive imager should allow for a deployment scheme wherein very little power is consumed, allowing for long useful deployments. The performance of the proposed device is evaluated with direct analysis and finite element simulations. Simulations predict that it will achieve comparable performance to today's commercial transducers, suggesting that the proposed device will be successful as an acoustic imager.

Contents

List of Figures

List of Tables

Chapter 1

Introduction

Remarkably, the National Oceanic and Atmospheric Administration estimates that less than 5% of the ocean has been explored to date, despite covering over 70% of the earth's surface and containing 97% of its water [1]. This is not for lack of motivation; we are well aware that the ocean is inextricably tied to climate and weather, and is home to some of the most exotic and diverse ecosystems on the planet. The study of these ecosystems has had notable effects that range from inspiring new medicines [2] to better understanding the carbon cycle [3], yet only about 10% of the estimated two million marine species have been discovered [4].

Outside of scientific exploration, there is also interest in ocean monitoring for commercial and military purposes. The ocean is a leading source of crude oil, and in order to keep up with ever-increasing demands, the oil industry has increasingly turned to offshore drilling in recent years. One-third of the world's oil output is now extracted offshore, and deepwater oil production alone has tripled from 1.5 to 4 million barrels per day between 2000 and 2010 [5]. The scale of these operations, along with difficulties associated with the harsh ocean conditions (e.g. high pressures, corrosion, bio-fouling), make them especially prone to destructive failure like the recent 210 million gallon Deepwater Horizon oil spill; improved monitoring is therefore crucial for the prevention and mitigation of future disasters. Oceans have also historically been exploited in military endeavors, where their sheer size makes them difficult to continuously and fully monitor, allowing for undetected enemy infiltration.

With a plethora of motivation, our exploration of the ocean is now limited by technology that is suitable for operation in the harsh ocean environment. Equipment that is robust to the high pressures at ocean depth is typically also expensive, so measurements are only taken at a single point and it is difficult to gather data with the required resolution. Furthermore, due to water conditions such as high salinity and low ambient lighting, standard sensors are typically inoperable in the ocean, meaning specialized technology must be developed.

1.1 Underwater Wireless Sensor Networks

An ideal ocean monitoring system has high temporal and spatial resolution over large regions. One well-suited approach that has recently received increasing attention is that of underwater wireless sensor networks (UWSNs) [6], which comprise potentially thousands of discrete nodes that use wireless telemetry to relay sensor readings. One well-known implementation of an UWSN is the Autonomous Oceanographic Surveillance Network (AOSN), which was developed by the Office of Naval Research [7]. AOSN uses a system of coordinated Autonomous Underwater Vehicles (AUVs) to scan a region of ocean. While an effective first step, the costly nature of AUVs limits the number of deployable nodes and therefore the spatial resolution.

Recently, there has been a growing interest in mobile UWSNs as an alternative to the coordinated-AUV UWSN [6]. As shown in figure 1.1, mobile UWSNs consist of untethered nodes and are deployed by scattering sensor nodes throughout an ocean region, leaving them free to migrate with fluctuating currents. The untethered nature of the nodes has two significant implications: no electrical connection is available, and retrieval of the nodes after deployment is impractical. The former dictates that the on-board devices consume very little power in order to achieve sufficiently long-duration useful deployments [8]. A consequence of the latter is that whatever is deployed into the ocean will stay there, so the materials that are used should be biodegradable and not harmful to ocean ecosystems [9]. It is furthermore desired that the node be capable of operation at full ocean depth, where hydrostatic pressures may exceed 1000 times the surface value. Together, the aforementioned factors presents sensor designers with a unique set of technological obstacles and places significant limitations on the available sensing technologies that are useful in UWSNs. One viable technology that is amenable to UWSNs, however, is that of acoustic sensing.

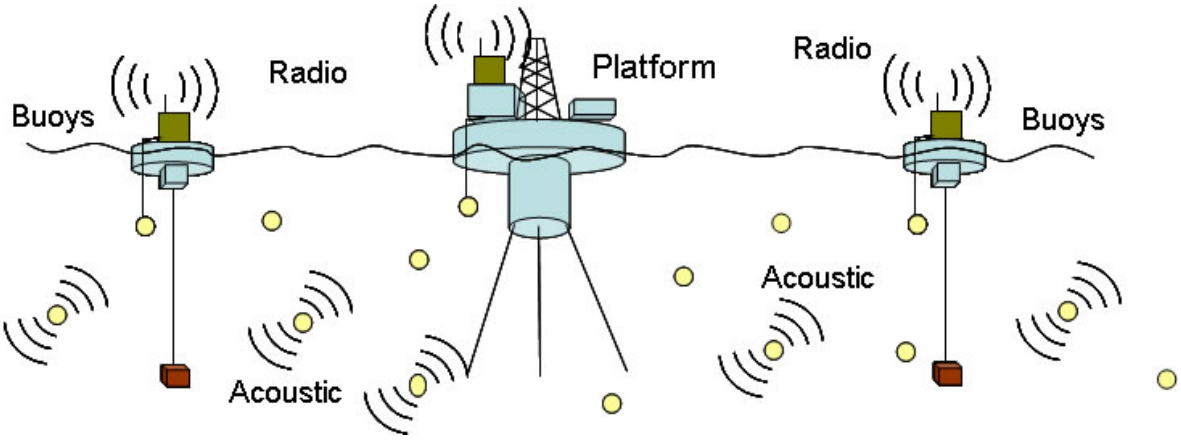

Figure 1.1: Conceptual illustration of a mobile UWSN [10]. Sensor nodes are untethered and scattered through a region, allowing for an inherently high spatial resolution. Readings are relayed wirelessly, typically using acoustics, to a central data processing unit such as a buoy station.

1.2 Underwater Acoustics and Imaging

One of the most powerful ways of observing an environment is to image it. However, the ocean environment is not conducive to standard imaging techniques, as optical and radio-frequency electromagnetic waves are attenuated quite rapidly. In fact, light absorption and scattering are so strong in the ocean that, even in the best conditions (e.g. shallow, clean waters) and with the most powerful light sources, transmission ranges are limited to just 200 meters [11]. In the context of UWSNs, however, high-power sources are impractical and water conditions are less than ideal, so typical lengths are only a small fraction of that limit.

Fortunately, the same limitation does not hold for acoustic waves, whose susceptibility to attenuation is some three orders of magnitude smaller than that of light waves [11]. Acoustic waves are additionally appealing because their relatively long wavelength make them insensitive to local water quality and small particulates [12]. These factors have been key to the successful and near-ubiquitous adoption of acoustics as a platform for underwater imaging technology.

All underwater imagers must employ transducers, the most common of which is far and away the electroacoustic transducer. This type of device, which will henceforth be referred to simply as an acoustic transducer, converts energy between the acoustical and electrical domains. Acoustic transducers may be designated broadly according to their designed function; *projectors* are used to electrically generate acoustic energy, and *hydrophones* are used to electrically sense acoustic energy. In certain situations, a given device may function well as both a projector and a hydrophone, but this is not always the case. Acoustic imagers are then comprised of an array of many individual transducers, similar to the way an array of individual pixels is used to create photographic images in a digital camera.

Acoustic imagers may also be separated into *active* and *passive* systems. Active imagers both create and sense acoustic energy in what is known as pulse-echo mode; they are operated briefly as a projector in order to generate acoustic pulses, then are switched to a "hydrophone mode" where they wait for the generated acoustic pulse to reflect off of objects and return to the array. The most common example of this technology is active SOund NAvigation and Ranging (SONAR), which was developed for military purposes in World War II [13]. Conversely, passive imagers utilize ambient acoustic energy to image their environment. One such system is the Acoustic Daylight Ocean Noise Imaging System (ADONIS) developed by Buckingham [14]. ADONIS uses ambient ocean noise, or "acoustic daylight," to create images in similar fashion to the way the human eye uses natural daylight: the acoustic energy generated from some distant source reflects off an object, and this reflection can be used to reconstruct an image. An illustrative comparison of active and passive imaging systems is provided in figure 1.2.

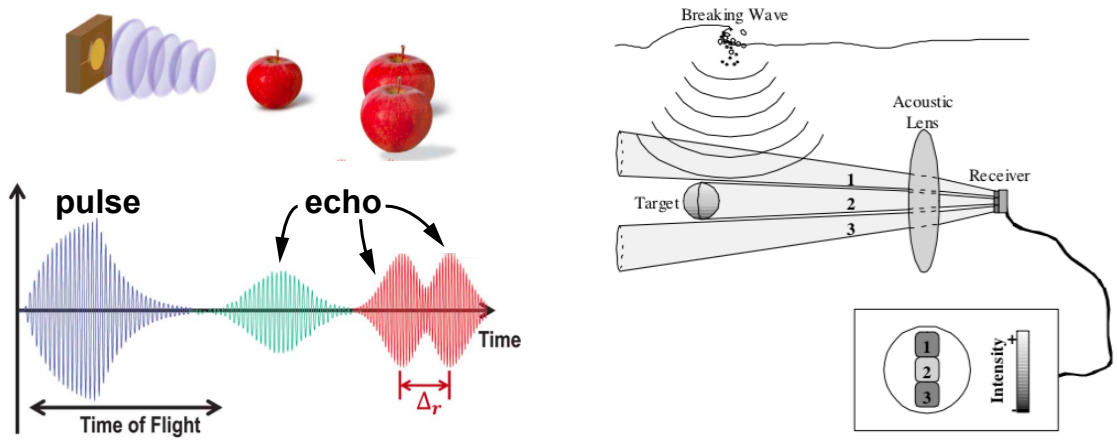

Figure 1.2: Conceptual schematic of active (left, adopted from [15]) and passive acoustic imaging (right, [14]). The passive imaging system shown here is based on ADONIS.

1.3 Performance Metrics

As acoustic imagers are made of an array of transducers, the performance of the system is strongly influenced by that of the individual elements. Presented here are a few salient metrics by which acoustic transducers are typically evaluated. Many of these metrics appear in the frequency response of the device, which is typically very reminiscent of a single degree of freedom mass-spring-damper system and is shown in figure 1.3.

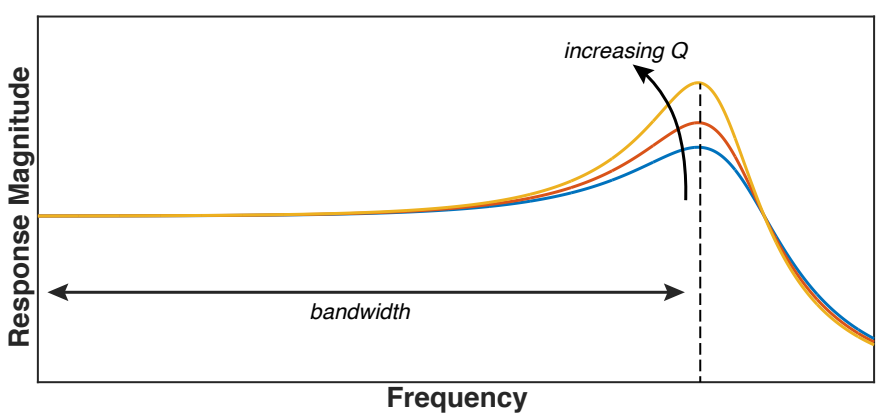

Figure 1.3: Qualitative frequency response plot of a typical acoustic transducer. Here the response of a hydrophone is defined as displacement per unit pressure in, and the response of a projector is defined as displacement per unit voltage in.

1.3.1 Bandwidth

A high bandwidth is desired for a few reasons. Neglecting the effects of electrical loading, the response of acoustic transducers is typically flat below resonance, so high bandwidth in a hydrophone means that it is capable of measuring acoustic signals across a wide range of frequencies without complex calibration. High bandwidth devices also tend to have better resolution since acoustic waves at higher frequencies have shorter wavelengths and can therefore resolve smaller objects.

1.3.2 Response Magnitude

In hydrophones, the response magnitude is often specified by the open-circuit voltage sensitivity (OCVS), or the electrical output per unit acoustic pressure input when connected to an infinite electrical impedance. In projectors, the response magnitude is generally specified by the transmitting voltage response (TVR), or the acoustic pressure output per unit electrical input. Therefore, a large response magnitude is desired in all cases.

1.3.3 Quality Factor

One definition of the quality factor, Q, is the ratio of the D.C. response magnitude to the resonance response magnitude. In general, a low Q is indicative of high damping, and in acoustic transducers, both the structural and surrounding mediums contribute to damping. High structural damping represents large internal losses in the device and is undesirable, but high damping from the surrounding medium is indicative of an efficient transfer of acoustic energy to and from the surrounding medium, which is desired in acoustic transducers. Therefore, it is desired to have a low Q, but it must *not* be due to a lossy structural material.

1.3.4 Robustness

The salinity of ocean water renders any electronics in contact with it inoperable, so protective layers must be incorporated into transducer designs. Additionally, the extreme pressures encountered at ocean depths pose a substantial difficulty for acoustic transducers and sensors in general. Acoustic transducers inherently have vibrating parts, which often require some kind of cavity and are therefore prone to blowout at high pressures. Furthermore, the transduction materials may behave differently or become unresponsive altogether at high pressures.

1.3.5 Beam pattern

The beam pattern, shown in figure 1.4, is used to characterize the directional response of hydrophones and projectors. The beam pattern is frequency dependent: the transducer is omnidirectional in nature at low frequencies (when the wavelength is large compared to the transducer), but at high frequencies main and side lobes are present. The beamwidth is generally defined as the 3 dB (half-power) angle of the main lobe, and it carries different significance for hydrophones and projectors. In hydrophones, beamwidth impacts resolution: narrower beams mean better source localization, which leads to higher resolution. In projectors, the beamwidth is important with respect to spreading losses. Spreading loss is a byproduct of conservation of energy; as the acoustic signal propagates and spreads, its intensity necessarily decreases accordingly. Projectors with narrow beam patterns are therefore required for long distance transmissions. Typically, transducer manufacturers either provide plots of the beam pattern or list the beamwidth at a few frequencies.

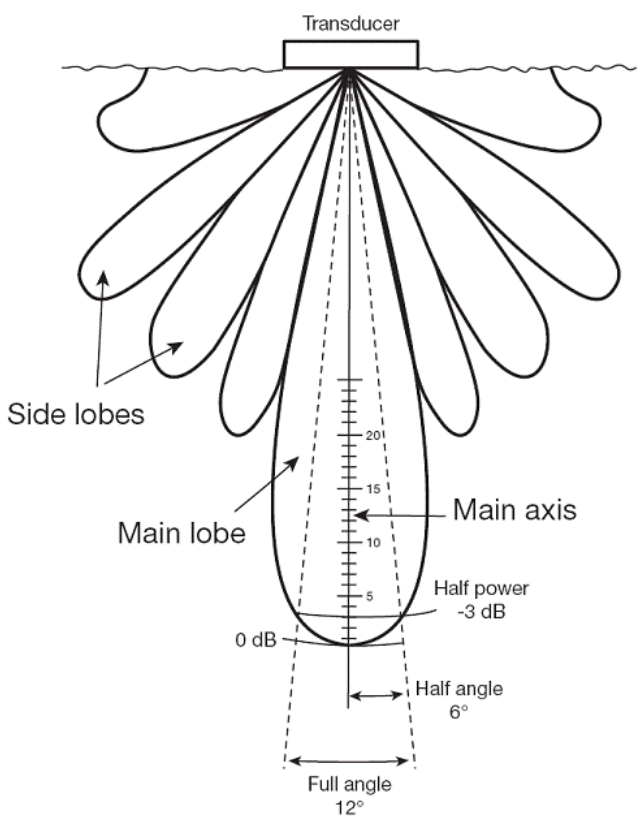

Figure 1.4: Illustrative description of an acoustic beam pattern [16]

1.4 Transducer Designs

1.4.1 The Tonpilz (Piston) Transducer

Since the advent of SONAR, the most prevalent acoustic transducer design has been the Tonpilz transducer [13]. It is often referred to as a piston transducer, as the radiating face ideally vibrates uniformly in a piston-like motion. Tonpilz transducers are typically designed to be an efficient projector so they have a high TVR, and the resulting hydrophone performance is found to be adequate. They are commercially available in a wide range of bandwidths beam patterns, and are therefore well-suited for a host of applications. As shown in figure 1.5, Tonpilz transducers tend to have many components, thus their manufacturing is complex, especially when attempting to make small devices. As a result, Tonpilz arrays are quite large and prohibitively expensive, eliminating them as a candidate technology for UWSNs.

1.4.2 Scaling Down

To be amenable to UWSNs, acoustic transducers must be small and capable of being mass-produced in array form. This set of requirements is uniquely well-suited for microelectromechanical systems (MEMS) and their standard batch fabrication methods. MEMS acoustic devices typically utilize a vibrating membrane and either capacitive or piezoelectric transduction for sensing and/or generating acoustic energy. These devices are termed capacitive or piezoelectric micromachined ultrasonic transducers (cMUT and pMUT, respectively). A pMUT array is illustrated in figure 1.6

While the development of both MUT technologies has received much attention, pMUT have emerged as a superior option in acoustic imaging, largely due to the requisite shallow cavity in cMUT which limits their range of motion. Accordingly, pMUT have been widely developed for acoustic applications, especially for medical imaging and consumer electronics. While they have shown various benefits in this context, including high TVR and OCVS, pMUT are limited by blowout issues under the hydrostatic pressures experienced in the ocean [17], and require costly ceramic piezoelectric materials.

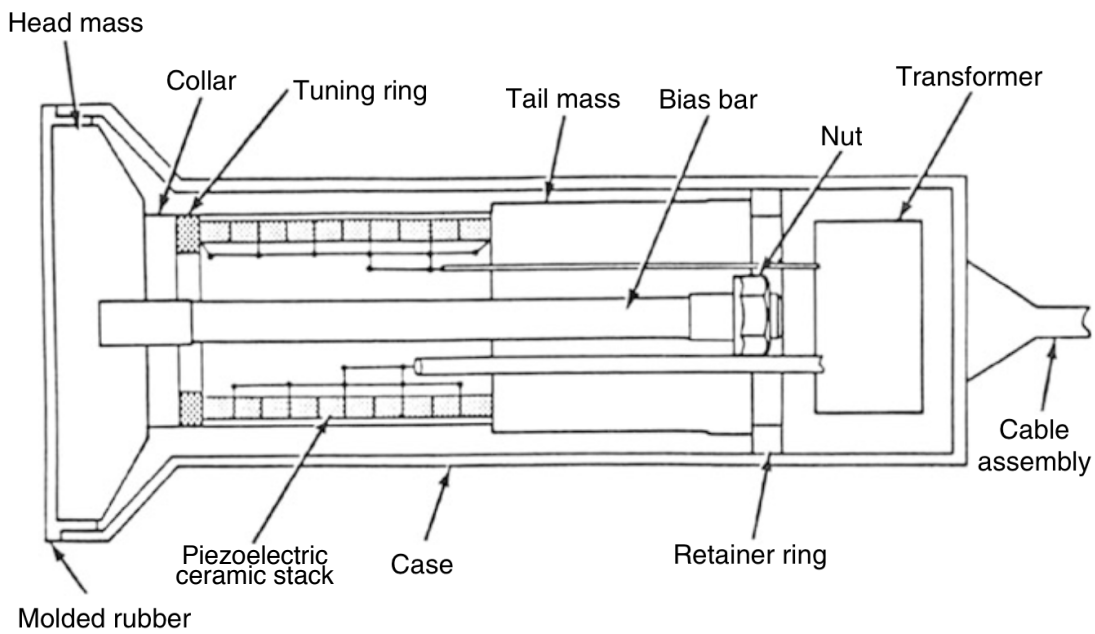

Figure 1.5: Schematic of a standard Tonpilz transducer (adapted from [13]).

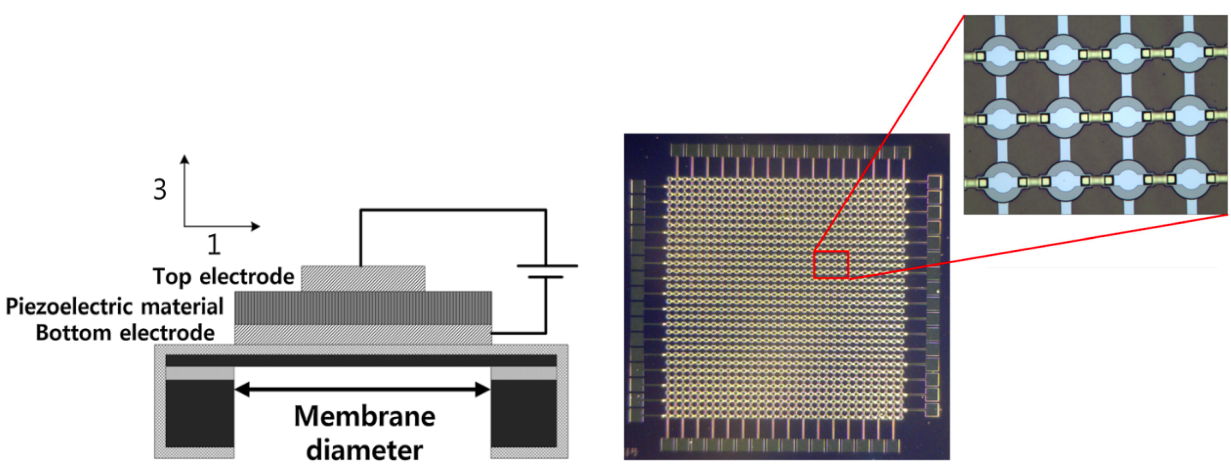

Figure 1.6: An individual pMUT (left) and an array of pMUT (right). Due to the use of standard microfabrication techniques, arrays of many transducers may be made at once.

1.5 Objectives and Proposed Device

The proposed device, shown in figure 1.7, is designed to fill the unique needs set forth by UWSNs. Its simple architecture lends itself to manufacturing with standard microfabrication techniques, thus relatively small-sized, low-cost arrays with many transducers may be made. The need for a diaphragm is eliminated by operating in a thickness-mode, making this structure more robust to the high pressures experienced at ocean depth. Additionally, the proposed transducer may act both as a passive and active imager; this will allow for a deployment scheme wherein the device operates in a passive low-power mode while capturing low-fidelity images until an event is detected, at which point it may be switched to an active mode in order to obtain high-resolution images. This should greatly reduce the power consumption when compared to transducers that are only suited for operation in one mode, and be an enabling technology for UWSNs.

Of course, in order to substantiate these claims the device must be analyzed. As such, the goals of this report are two-fold: (1) to present and compare methods of analysis of the proposed device, and (2) to verify its viability as an option for acoustic imaging in UWSNs.

The motivation for the first goal is as follows. Due to the complexities associated with mathematical analysis of acoustics, devices are often designed solely by "rules of thumb," and then characterized post-fabrication [18]. Analytical approximations are available, but their conditions for validity have not been broadly studied, thus diminishing their general usefulness for transducer designers. With the emergence of finite element modeling, the tools are now available to tackle complex problems where analytic methods fail. The two methods of direct analysis and finite element modeling will be compared in this report in order to suggest when the simplified analysis may be sufficient, and when the more burdensome finite element approach should be taken. The second goal will be achieved by simulating some of the performance metrics listed in section 1.3

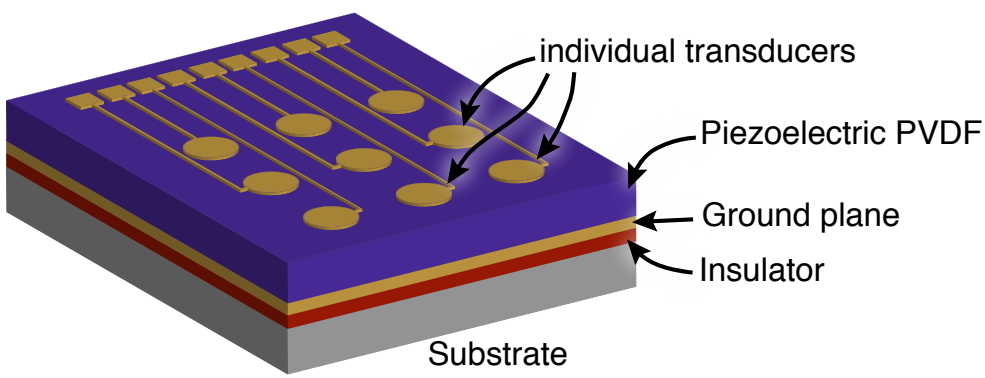

Figure 1.7: Schematic of the proposed device. Not shown: Parylene-C coating for isolating electronics from environment.

1.6 Report Outline

This report is organized into four chapters as follows. Chapter 1 has motivated the development of acoustic imagers for UWSNs, including the introduction of some of the metrics by which acoustic transducers are evaluated. Chapter 2 covers the governing transduction physics, namely acoustics and piezoelectricity, which are then used to present the one-dimensional analysis of transducers via a lumped-parameter circuit. Finite element models in COMSOL Multiphysics are developed in Chapter 3, and their results are used to predict the response of both hydrophones and projectors. Furthermore, the results are compared to the predictions made by the one-dimensional analysis. Finally, in Chapter 4, conclusions based on the presented work are offered, and the next steps in this project are suggested.

Chapter 2

Transduction Physics, Analysis and Materials

Fundamental to the operation and performance of acoustic transducers is an understanding of the governing physics and a consideration of common materials used. In this chapter, solutions to the acoustic wave equation are offered, including identification of the all-important acoustic impedance and an examination of the acoustic transmission across an interface of dissimilar materials. The piezoelectric effect, which couples structural deformations and electric fields, is summarized and the constitutive equations are presented. Common piezoelectric transducer materials are compared and focus is given to Polyvinylidene Fluoride (PVDF), which is emerging as an appealing alternative to the classically used ceramics. The chapter concludes with the derivation and exploration of an analytical transducer model, which is used to identify some required changes to the proposed transducer architecture.

2.1 Acoustics

Fundamentally, an acoustic wave is a mechanical perturbation propagating through a medium. One way to derive acoustic equations is to begin with the stresses on a differential mechanical element, as displayed in figure 2.1 [18].

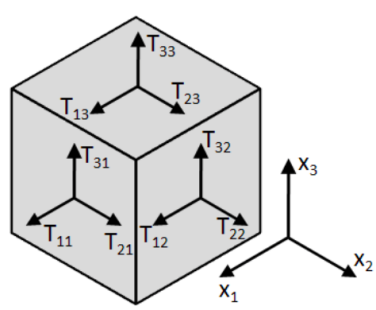

Figure 2.1: Stresses on a differential mechanical element [18].

In an elastic, isotropic medium the labeled stresses are related to the strains by eq 2.1

$$\begin{bmatrix} T_1 \\ T_2 \\ T_3 \\ T_4 \\ T_5 \\ T_6 \end{bmatrix} = \begin{bmatrix} \lambda+2\mu & \lambda & \lambda & 0 & 0 & 0 \\ \lambda & \lambda+2\mu & \lambda & 0 & 0 & 0 \\ \lambda & \lambda & \lambda+2\mu & 0 & 0 & 0 \\ 0 & 0 & 0 & \mu & 0 & 0 \\ 0 & 0 & 0 & 0 & \mu & 0 \\ 0 & 0 & 0 & 0 & 0 & \mu \end{bmatrix} \begin{bmatrix} S_1 \\ S_2 \\ S_3 \\ S_4 \\ S_5 \\ S_6 \end{bmatrix} \tag{2.1}$$

$$\begin{array}{ll} T_{11} = T_1 & T_{23} = T_{32} = T_4 \\ T_{22} = T_2 & T_{13} = T_{31} = T_5 \\ T_{33} = T_3 & T_{12} = T_{21} = T_6 \end{array}$$

Where T denotes stress, S denotes strain, and λ and μ are the first and second Lamé constants, respectively. It should be noted that the second Lamé constant is a measure of the shear modulus of a material, thus $\mu = 0$ in all fluids. The first Lamé constant, however, is related to the Young's modulus, Bulk modulus, and Poisson ratio of the medium. Applying Newton's second law to the differential element in figure 2.1 and assuming motion is restricted to the x_3 direction, the equation of motion can be derived as [18]

$$\frac{\partial T_3}{\partial x_3} + \frac{\partial T_4}{\partial x_2} + \frac{\partial T_5}{\partial x_1} = \rho \frac{\partial^2 u_3}{\partial t^2} \tag{2.2}$$

Where u_3 is the particle displacement in the x_3 direction and ρ is the mass density (kg/m^3). In the case of a plane longitudinal wave, all shear stresses and strains are eliminated and eqs 2.1 and 2.2, respectively, reduce to

$$T_3 = (\lambda + 2\mu) S_3 = (\lambda + 2\mu) \frac{\partial u_3}{\partial x_3} \tag{2.3}$$

$$\frac{\partial T_3}{\partial x_3} = \rho \frac{\partial^2 u_3}{\partial t^2} \tag{2.4}$$

It is now apparent that T_3 is equal and opposite to the acoustic pressure, p, since positive T_3 corresponds to tension and positive p corresponds to compression. Upon substitution, eqs 2.3 and 2.4 simplify to the wave equation that governs one-dimensional acoustics:

$$\frac{\partial^2 u_3}{\partial x_3^2} = \frac{\rho}{\lambda + 2\mu} \frac{\partial^2 u_3}{\partial t^2} \tag{2.5}$$

Where it is apparent that eq 2.5 represents a wave with propagation velocity $c = \sqrt{\rho/(\lambda + 2\mu)}$. The general solution to eq 2.5 is the sum of any left- and right-traveling functions:

$$u_3(x_3, t) = u_3^+(x_3 - ct) + u_3^-(x_3 + ct) \tag{2.6}$$

Note also that the wavelength λ, sound speed c, and frequency f are related by

$$c = f\,\lambda \tag{2.7}$$

2.1.1 Acoustic Impedance

It is well known that steady state acoustic waves are harmonic both in time and space, thus an exponential form is assumed

$$u_3^+ = u_{3,0}^+ e^{j(\omega t - kx)} \tag{2.8}$$

With a similar form being taken for u_3^-. Eq 2.8 represents a phasor solution to particle displacement, thus the particle velocity may be obtained by taking the time derivative

$$v_3 = \frac{\partial u_3}{\partial t} = j\omega u_3 \tag{2.9}$$

In order to fulfill the requirements set forth by the general solution, eq 2.5, it must be the case that the wavenumber $k = \omega/c$. The spatial derivative of particle displacement can then be written as

$$\frac{\partial u_3}{\partial x_3} = -jku_3 \tag{2.10}$$

Combining eqs 2.3, 2.9, and 2.10 relates the acoustic pressure and particle velocity. This yields the so-called specific acoustic impedance, which will prove to be a critical value for transducers:

$$Z = \frac{p}{v_3} = \rho c \tag{2.11}$$

Z is termed the *specific* acoustic impedance because it is an intrinsic property of the medium; it does not depend on any geometric parameters. It has units of kg/m^2/s, commonly referred to as a Rayleigh (1 kg/m^2/s=1 rayl). For reference, the specific acoustic impedance of water and steel are about 1.5 and 47 Mrayl, respectively. In general, materials that are dense and have large elastic constants have high specific acoustic impedances.

2.1.2 Acoustic Transmission Across the Interface of Two Materials

The functionality of acoustic transducers necessarily requires them to interact with the acoustic field. Since the transducers are not made of water, they represent an interface in materials, so it is important to consider how this might impact the performance of the device. While an analytic solution is not possible for the general case, the simple 1-dimensional case shown in figure 2.2 can provide valuable relevant intuition.

In this analysis, perfect plane waves and an exactly straight interface at $x = y$ are assumed. Following eq 2.6, there may simultaneously exist two opposing acoustic waves; here the right- and left-moving pressure waves in regions 1 and 2, respectively, are defined as $\mathcal{F}_{1,2}(x - c_{1,2}t)$ and

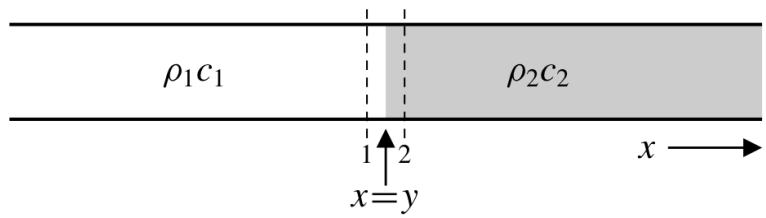

Figure 2.2: Schematic of setup used for analysis of acoustic transmission across a material interface [19].

$\mathcal{G}_{1,2}(x + c_{1,2}t)$. Applying continuity of velocity and pressure along the interface, and conservation of mass to two control volumes enclosing the interface, yields the jump conditions for the system. Furthermore, it can be shown that if a source exists at $x < y$ that generates $\mathcal{F}_1$ in an infinitely long tube (so that $\mathcal{G}_2 = 0$), the three waves are related by [19]

$$\mathcal{G}_1(x + c_1 t) = R_A \mathcal{F}_1\big(2y - (x + c_1 t)\big) \tag{2.12}$$

$$\mathcal{F}_2(x - c_2 t) = T_A \mathcal{F}_1\big((1 - \frac{c_1}{c_2})y + \frac{c_1}{c_2}(x - c_2 t)\big) \tag{2.13}$$

$$R_A = \frac{\rho_2 c_2 - \rho_1 c_1}{\rho_2 c_2 + \rho_1 c_1}, \quad T_A = \frac{2\rho_2 c_2}{\rho_2 c_2 + \rho_1 c_1} \tag{2.14}$$

For the acoustic transducers considered in this report, the transmission coefficient, T_A, is of the utmost importance; T_A relates the rightward acoustic waves $\mathcal{F}_1$ and $\mathcal{G}_1$ and is thus a measure of the amount of acoustic energy transferred between the two mediums. Considering a hydrophone, for example, if the acoustic energy never enters the transducer then it cannot possibly detect that energy, rendering the device useless. For this reason, it is desired to maximize T_A. As can be seen in eq 2.14, $T_A = 1$ and $R_A = 0$ when $\rho_1 c_1 = \rho_2 c_2$; it is therefore critical that the transducer be "impedance matched" to its environment.

2.2 Piezoelectric effect and its constitutive equations

The piezoelectric effect is defined as the formation of electrical charges from an applied force, and vice-versa. It is present only in crystalline solids which lack a center of inversion symmetry, which is to say their crystal structure is non-symmetric with respect to some point. Piezoelectric materials are extremely useful in underwater acoustic transducers because of their ability to generate large forces at high frequencies without applying a bias voltage, the simplicity of their implementation, and their minimal losses [13].

In order to model piezoelectricity, the standard stress-strain relationships given in eq 2.1 must be adopted to account for the electromechanical coupling. These modified equations may take several equivalent forms. The so-called *d-form* is defined by

$$\begin{bmatrix} S_1 \\ S_2 \\ S_3 \\ S_4 \\ S_5 \\ S_6 \end{bmatrix} = \begin{bmatrix} s_{11}^E & s_{12}^E & s_{13}^E & 0 & 0 & 0 \\ s_{21}^E & s_{22}^E & s_{23}^E & 0 & 0 & 0 \\ s_{31}^E & s_{32}^E & s_{33}^E & 0 & 0 & 0 \\ 0 & 0 & 0 & s_{44}^E & 0 & 0 \\ 0 & 0 & 0 & 0 & s_{55}^E & 0 \\ 0 & 0 & 0 & 0 & 0 & s_{66}^E \end{bmatrix} \begin{bmatrix} T_1 \\ T_2 \\ T_3 \\ T_4 \\ T_5 \\ T_6 \end{bmatrix} + \begin{bmatrix} 0 & 0 & d_{31} \\ 0 & 0 & d_{32} \\ 0 & 0 & d_{33} \\ 0 & d_{24} & 0 \\ d_{15} & 0 & 0 \\ 0 & 0 & 0 \end{bmatrix} \begin{bmatrix} E_1 \\ E_2 \\ E_3 \end{bmatrix}$$

$$\begin{bmatrix} D_1 \\ D_2 \\ D_3 \end{bmatrix} = \begin{bmatrix} 0 & 0 & 0 & 0 & d_{15} & 0 \\ 0 & 0 & 0 & d_{24} & 0 & 0 \\ d_{31} & d_{32} & d_{33} & 0 & 0 & 0 \end{bmatrix} \begin{bmatrix} T_1 \\ T_2 \\ T_3 \\ T_4 \\ T_5 \\ T_6 \end{bmatrix} + \begin{bmatrix} \varepsilon_{11}^T & 0 & 0 \\ 0 & \varepsilon_{22}^T & 0 \\ 0 & 0 & \varepsilon_{33}^T \end{bmatrix} \begin{bmatrix} E_1 \\ E_2 \\ E_3 \end{bmatrix} \tag{2.15}$$

Where subscripts denote direction, and superscript E and T denote that a parameter is measured under constant electric field or temperature conditions, respectively. E refers to electric field, and D refers to electric charge density displacement. Elastic compliance is given by the s terms, ε terms are the dielectric constants, and the d terms are the piezoelectric constants. As before, T and S respectively refer to stress and strain. It should be noted that the compliance matrix is directly related to the stiffness matrix introduced in eq 2.1; it has not changed as a byproduct of the piezoelectric effect.

2.3 Materials

Piezoelectricity was first discovered in quartz in 1880 by the Curie brothers [13], which is still one of the most widely used piezoelectrics. Despite the attractive qualities of quartz, the underwater acoustic community has, and continues to, relentlessly develop new piezoelectric materials with larger responses and improved performance.

The era of "modern" transducers began in the 1940's, when piezoelectricity began being discovered in more exotic ceramics. In 1944 strong piezoelectricity was discovered in barium titanate ceramics, followed by even stronger piezoelectricity in lead zironate titanate (PZT) in 1954 [20]. Since its discovery, PZT has become the gold standard in transducer design, and is by far the most commonly used piezoelectric in this application today. PZT is not perfect, however, especially in regards to thickness-mode devices. As a very stiff and dense material, PZT has an acoustic impedance many times that of water and thus internally reflects most acoustic energy, largely

negating the benefits of its improved piezoelectricity. The acoustic impedance mismatch between water and PZT or other ceramics has motivated a shift in the focus in material development to include piezoelectric polymers, most notably Polyvinylidene Fluoride (PVDF).

PVDF is a fluoropolymer whose piezoelectricity was discovered by Heiji Kawai in 1969 [21], and has since become established as one of the most commonly used materials in acoustic imaging devices. It typically exists in two phases: α or β (see Figure 2.3). In the β phase, the hydrogen and fluorine atoms exist on opposite sides of the carbon backbone. The difference in their electronegativies creates an electric dipole, so β-phase PVDF responds to an applied electric field and therefore exhibits piezoelectricity. Unprocessed PVDF samples are not piezoelectric, as they contain both phases and the β-phase that is present is randomly oriented. In general, PVDF is made piezoelectric by a combination of mechanical stretching and electrical poling (i.e. applying a large electric field), which limits its use to thin sheets [22].

A comparison of relevant material parameters for PZT and PVDF is given in table 2.1, where it can be seen that PVDF exhibits an almost 10$\times$ better impedance match with water than PZT. This benefit alone is enough to outweigh the negative implications of its comparatively low permittivity, high mechanical losses (low Q), and low piezoelectric constants. In order to get similar performance out of PZT devices, complex designs and multiple impedance-matching layers are required [18]. Aside from its acoustic impedance, PVDF has several additional advantageous properties. Firstly, while ceramics are prone to de-poling (losing piezoelectric properties) at high pressures, PVDF is not [13]. This makes PVDF ideal for deep-sea applications. The outstanding mechanical flexibility of PVDF also lends itself to non-planar geometries, which has interesting implications on acoustic focusing [23]. Commercially available PVDF also has a substantially lower cost than piezoelectric ceramics [24], and implementation involves relatively simple fabrication steps.

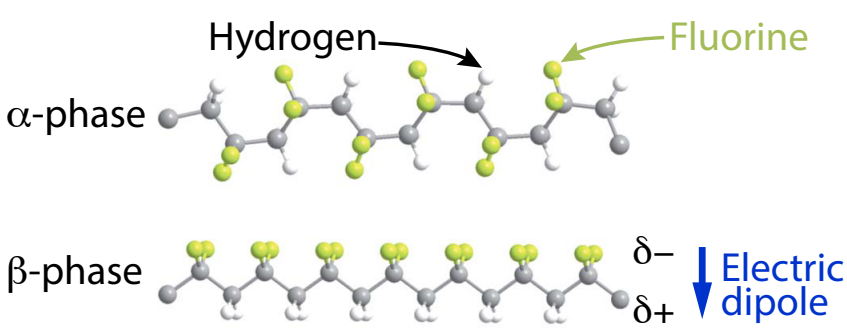

Figure 2.3: The atomic structure of PVDF. In the β-phase the difference in electronegativity between hydrogen and fluorine creates an electric dipole, making the material piezoelectric (adopted from [25]).

Table 2.1: Comparison of piezoelectric transduction materials [26], [27].

Parameter	**PZT-5A**	**PVDF**
Sound speed (m/s)	4350	2200
Density (kg/m^3)	7750	1780
Z (Mrayl)	33.7	3.9
Z/Z_w	24.1	2.8
Relative permittivity $\varepsilon/\varepsilon_0$	1200	8-12
Mechanical Q	75	10
Piezoelectric constant d_{33} (10^{-12} C/N or m/V)	300	33
Mechanical Flexibility	Poor	Outstanding

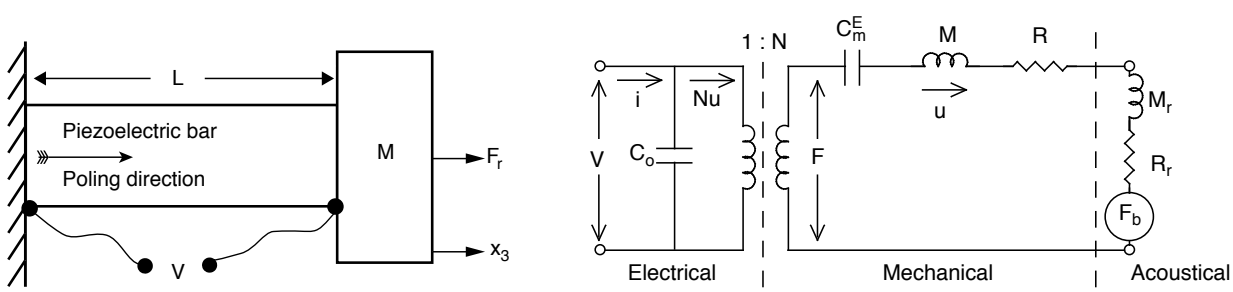

Figure 2.4: Schematic (left) and lumped-parameter circuit (right) for a one-dimensional longitudinal transducer [13].

2.4 The One-Dimensional Transducer

The performance of acoustic transducers is typically analyzed with a one-dimensional, lumped-parameter approach. By definition, the piezoelectric is poled in the x_3 direction, and when motion into the acoustic medium is in the same direction, the device is termed a *longitudinal* transducer. A schematic of such a device given in figure 2.4. In this configuration, only the head mass M is in contact with the acoustic medium, so strains (displacements) in the x_1 and x_2 directions play no role in the device performance. The piezoelectric equations (eq 2.15) can then be simplified:

$$S_3 = s_{33}^E T_3 + d_{33} E_3 \tag{2.16}$$

$$D_3 = d_{33} T_3 + \varepsilon_{33}^T E_3 \tag{2.17}$$

When the piezoelectric bar is short compared its acoustic wavelength, a constant stress T_3 may be assumed. Additionally assuming the displacement x_3 is small, the equation of motion for the bar may be written as

$$(M + M_r)\ddot{x_3} + (R + R_r)\dot{x_3} + \frac{A_0}{s_{33}^E L} x_3 = \frac{A_0 d_{33}}{s_{33}^E L} V + F_b \tag{2.18}$$

where F_b is an external force, such as an acoustic wave generated from an outside source. Eq 2.18 reveals the transformer turns ratio, which relates the applied voltage to generated force:

$$N = \frac{A_0 d_{33}}{s_{33}^E L} \tag{2.19}$$

Furthermore, eq 2.18 shows that mass and resistance (damping) are not solely determined by the transducer's mechanical properties - they also contain acoustic radiation parameters. The radiation mass and resistance, M_r and R_r, are artifacts of the acoustic medium providing a reaction force on the transducer:

$$\frac{F_r}{v} = -\frac{1}{v} \iint_S p(\vec{r})\, dS = -\big(R_r + j\omega M_r\big) \tag{2.20}$$

where $v = \dot{x_3}$ is the velocity of the surface of the transducer. The role of radiation resistance is entirely different from that of a typical resistance; mechanical resistance R represents a loss of energy inside a transducer, while the radiation resistance R_r is associated with the transfer of energy from the transducer to the acoustic medium. For this reason, it is desired that R is small but R_r is large.

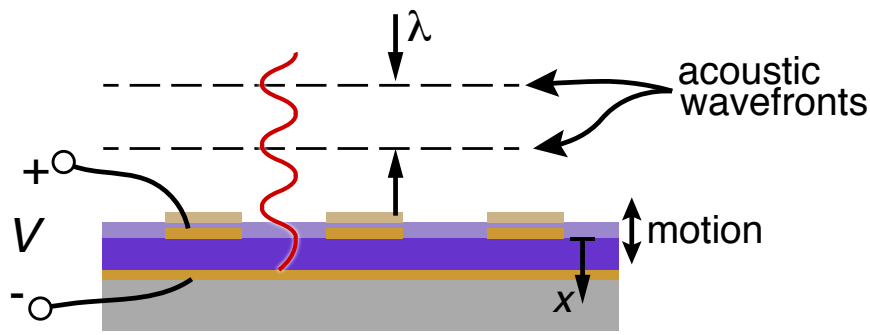

Figure 2.5: Schematic of device operation. The piezoelectric thickness is comparable to the acoustic wavelength, thus the constant-stress assumption is invalid.

2.4.1 The Mason Model

The preceding analysis is valid only for devices in which the piezoelectric layer is much smaller than the acoustic wavelength; this is typical for low-frequency transducers which have a sizable headmass and a radiating area that is larger than the piezoelectric area. In the interest of increasing the bandwidth of devices, however, PVDF transducers are designed to operate in conditions where their thickness is comparable to the acoustic wavelength, as shown in figure 2.5.

By combining eqs 2.6, 2.8, and 2.9, separating time and space-harmonic components, the acoustic particle velocity may be written as [13]

$$v(x) = j\omega\left(u_0^+ e^{-jkx} + u_0^- e^{jkx}\right) \tag{2.21}$$

where, for simplicity, the subscript 3 has been dropped and x refers to depth into the piezoelectric. The force, which is related to the stress and transducer area by $F = -A_0 T_3$, can then be written as

$$F(x) = -jkc_{33}\left(u_0^+ e^{-jkx} - u_0^- e^{jkx}\right) \tag{2.22}$$

where $c_{33} = 1/s_{33}$ is the elastic stiffness. At this point, u_0^+ and u_0^- remain unknown constants; in order to solve for them, it is convenient to define the mechanical impedance:

$$Z(x) = \frac{F(x)}{v(x)} = \rho c A_0 \frac{u_0^+ e^{-jkx} - u_0^- e^{jkx}}{u_0^+ e^{-jkx} + u_0^- e^{jkx}} \tag{2.23}$$

It is important to note that in acoustics an infinite medium is one in which there are no reflections. In such a domain, there is only one wave present (i.e., either u_0^+ or u_0^- are 0), and the mechanical impedance is closely related to the specific acoustic impedance:

$$Z(x) = \rho c A_0 \tag{2.24}$$

Note that here the units of mechanical impedance are Rayl m^2. If the boundary impedances are given by $Z(x = 0) = Z_0$ and $Z(x = L) = Z_L$, where L is the PVDF thickness, eq 2.23 may be manipulated to derive the so-called transmission line equation:

$$Z_0 = \rho c A_0 \frac{Z_L + j\rho c A_0 \tan(kL)}{\rho c A_0 + j Z_L \tan(kL)} \tag{2.25}$$

Eqs 2.24 and 2.25 can be used to define the "Mason model" of thickness-mode vibrations [28], shown in figure 2.6 with impedances

$$Z_a = j\rho c A_0 \tan(kL/2) \tag{2.26}$$
$$Z_b = -j\rho c A_0 \csc(kL) \tag{2.27}$$

Both the water and substrate are considered to be infinite domains in this model; this is true by virtue of its size for the surrounding water, and is a good approximation for the substrate since anechoic backing layers are usually used in transducers, eliminating reflections. The turns ratio N is consistent with eq 2.19, but is often rewritten in terms of the electric conversion coefficient, a different piezoelectric constant [29]:

$$N = h_{33} C_0 \tag{2.28}$$

where C_0 is the clamped capacitance of the transducer:

$$C_0 = \frac{\varepsilon_{33}^T A_0}{L} \tag{2.29}$$

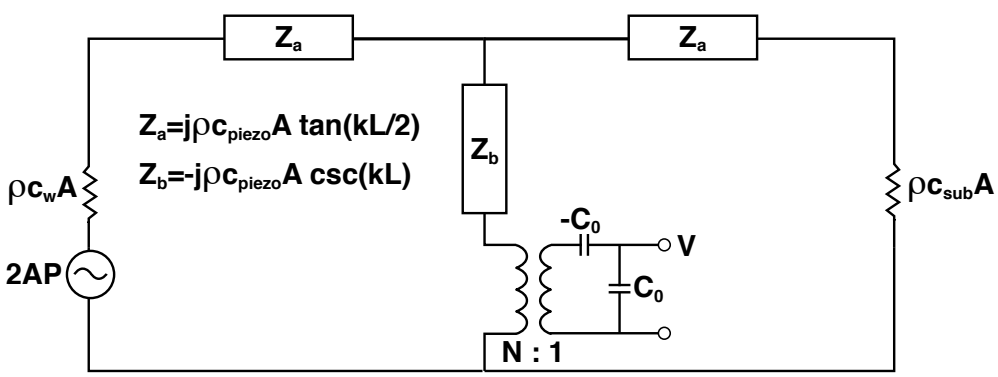

Figure 2.6: Thickness-mode "Mason"circuit of a PVDF transducer. In hydrophone operation, the left-hand source is the acoustic pressure and the output is voltage. When operating as a projector, the voltage is applied, and the pressure source is set to 0.

2.4.2 Resonance Conditions

Transducers are of little use beyond resonance due to the decay in their response, so it is important to analyze the resonance predicted by the Mason model, which can be done by examining eq 2.25. Resonance is defined as the mechanical impedance at the water-transducer interface, Z_0, reaching a minimal value.

In the case of PVDF attached to a high impedance substrate (e.g., silicon), $Z_L \gg \rho c A_0$, creating a clamped boundary condition and $Z_0 = j\rho c A_0 \cot(kL)$. Accordingly, the first resonance occurs when $Z_0 = 0$ at $kL = \pi/2$, or when $f = c/4L$, which is termed the quarter-wave or $\lambda/4$ resonance mode (see figure 2.7). Converseley, if the piezoelectric has a very high specific acoustic impedance (e.g., PZT), then $Z_L \ll \rho c A_0$ and both boundary conditions are free. In this case, $Z_0 = j\rho c A_0 \tan(kL)$ and the first resonance occurs at $kl = \pi$, or when $f = c/2L$, which is termed the half-wave resonance mode.

There are two salient characteristics of the $\lambda/2$ mode of operation that make it inherently less sensitive than the $\lambda/4$ mode. Firstly, the half-wave mode corresponds to a high impedance (stiff) material so the piezoelectric deforms very little, which greatly decreases the low-frequency response. Furthermore, since the displacement is anti-symmetric (e.g., half of the material is in tension, half is in compression), the transducer actually reaches its peak sensitivity well below resonance. As displayed in figure 2.8, these two facts greatly limit the bandwidth and decrease the sensitivity of devices that operate in the half-wave mode, thus thickness mode devices should almost always be designed for quarter-wave operation.

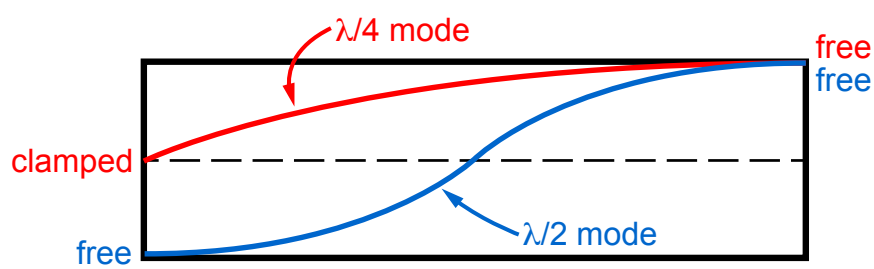

Figure 2.7: Illustration of thickness-mode transducer resonances. PVDF exhibits a $\lambda/4$ resonance on typical substrates, whereas most other piezoelectrics have high impedances compared to the substrate, and consequently operate in the $\lambda/2$ mode.

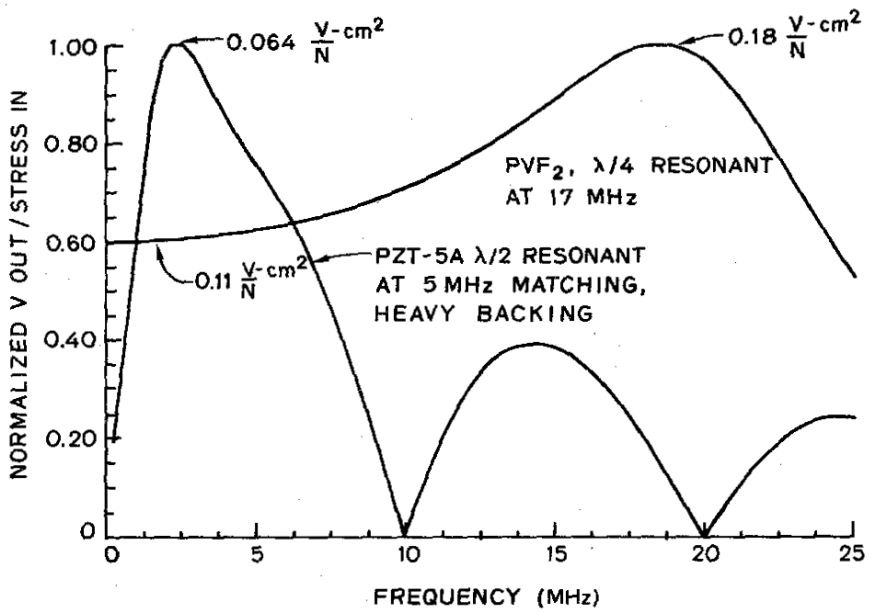

Figure 2.8: Comparison in performance of PZT and PVDF thickness-mode transducers [30]. The peak sensitivity of a PVDF hydrophone is about 3 times that of PZT, and it is sensitive over a much larger bandwidth.

2.4.3 Projector Beam Pattern

In general, the acoustic pressure generated by a vibrating surface is determined by the Rayleigh integral [31]

$$p(\vec{r}) = \frac{j\rho ck}{2\pi} \iint_S v(\vec{r_0}) \frac{e^{-jkR}}{R} \, dS \tag{2.30}$$

where $\vec{r}$ is the position vector to a point of interest in the acoustic medium, $\vec{r_0}$ is the position vector along the surface which is vibrating with velocity $v(\vec{r_0})$, and R is the distance from the differential surface element to the point of interest, which are labeled in figure 2.9.

Eq 2.30 may only be evaluated for a select list of situations, but one such case is relevant for the one-dimensional analysis presented here: the far-field radiation from a uniformly vibrating "piston" transducer in an infinite acoustic baffle. In this case, eq 2.30 simplifies to [13]

$$p(r, \theta) = j\rho cka^2 v_0 \frac{e^{-jkr}}{r} \frac{\mathrm{J}_1\big(ka \sin\theta\big)}{ka \sin\theta} \tag{2.31}$$

where J_1 is the first-order Bessel function. The velocity v_0 may be obtained by analyzing the Mason circuit in figure 2.6

$$v_0 = \frac{NV_{in}}{\rho c_w A_0 + Z_a + Z_b - N^2/(j\omega C_0)} \tag{2.32}$$

Generated acoustic pressures typically span several orders of magnitude, so it is convenient to define the acoustic pressure intensity L_p in decibels (dB) by

$$L_p = 10 \log_{10} \left(\frac{p_{rms}^2}{p_{ref}^2} \right) \tag{2.33}$$

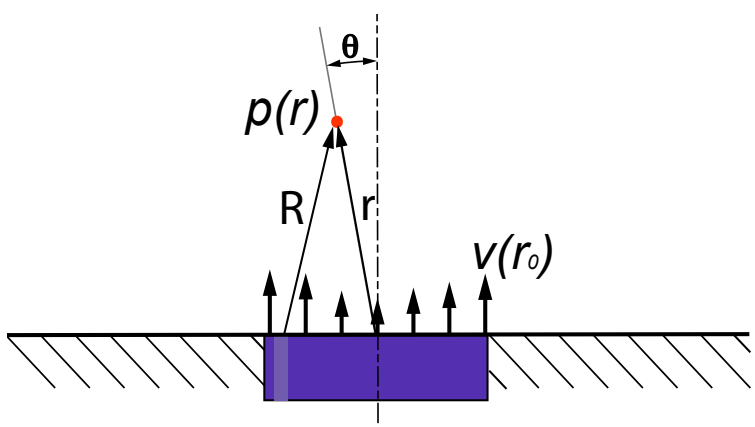

Figure 2.9: Definitions used for Rayleigh integral evaluation

where the reference pressure p_{ref} is arbitrary but is typically chosen as $1\,\mu$Pa in water. Similarly, the transmitting voltage response (TVR) is determined by dividing the argument of eq 2.33 by the input voltage:

$$TVR = 10\log_{10}\left(\frac{p_{rms}/V_{in}}{1\,\mu\text{Pa/V}}\right)^2 \tag{2.34}$$

Combining eqs 2.31-2.34 allows calculation of the radiated acoustic pressure as a function of angle θ, the so-called *transmitting beam pattern*. This is plotted in figure 2.10 for a $100\,\mu$m thick transducer with material constants defined according to table 3.2 and various radii.

Figure 2.10 displays the influence of the acoustic wavelength on the transducer behavior. For reference, $\lambda = 5$, 1.5, and 0.5 mm for $f = 300$ kHz, 1 MHz, and 3 MHz respectively. At lower frequencies, the diameter of the smaller transducer is much less than the acoustic wavelength, so it behaves in similar to a point source: it is omni-directional. The larger transducer is almost omni-directional at 300 kHz, but there is about a 10 dB difference between the θ =0 and θ =90° acoustic pressures. As the frequency increases and the transducer size becomes comparable to the wavelength, the acoustic energy generated by different portions of the transducer may interfere destructively at certain angles, thus creating acoustic pressure nulls. In general, larger transducers create more Furthermore, as can be seen in figure 2.10 and derived in eq 2.31, the maximum pressure always occurs at θ=0°, and for this reason the axial center is termed the maximum response axis (MRA).

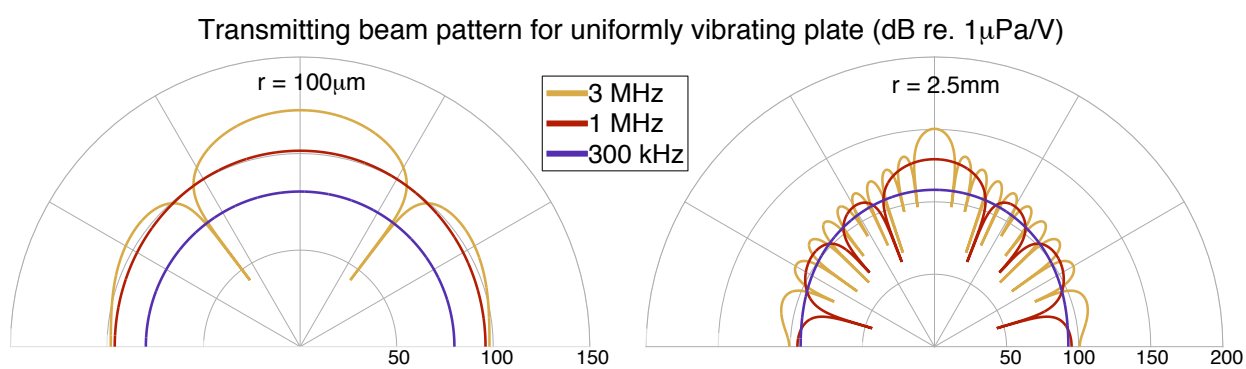

Figure 2.10: Theoretical transmitting beam pattern from a uniformly vibrating plate with radius $100\,\mu$m (left) and 2.5 mm (right)

2.4.4 Effects of Electrical Loading

When operating a transducer as a hydrophone, it is necessary to buffer the output signal. This is typically done with a high input-impedance device, such as an op-amp, to minimize electrical loading effects. Neglecting the (generally small) resistances, a hydrophone and its output buffer circuit can be drawn as in figure 2.11 [30]. If the transducer is connected to an infinite-impedance (i.e., zero capacitance) load, the measured voltage equals the Mason circuit voltage: $V_s = V_{out}$. However, the op-amp input capacitance C_{in} and parasitic capacitance C_p of connections to the hydrophone (e.g., lead lines, bondpads, connecting cables, etc.) are both present, which set up a potential divider. The output voltage of the buffer circuit, assuming an ideal op-amp aside from its nonzero capacitance, is given by

$$\frac{V_s}{V_{out}} = \frac{C_0}{C_0 + C_p + C_{in}} \tag{2.35}$$

The implications of eq 2.35 are critical to transducer performance and design. Firstly, a trade-off between resolution and sensitivity is presented; transducer size is typically decreased in order to increase resolution, however this also decreases C_0 and therefore the sensitivity. Also displayed in eq 2.35 is an inherent drawback of using PVDF; due to its relatively low dielectric constant, the transducer capacitance is comparable to the op-amp capacitance. By way of example, a $100\,\mu$m thick, 1 mm radius PVDF transducer has capacitance $C_0 = 3$ pF, whereas $C_{in} = 1 - 10$ pF for most op-amps (C_p varies widely). The potential division created by the input capacitance alone can therefore be significant, and the the parasitics only exacerbate the problem. To prevent substantial signal degradation, the transducer array design should aim at minimizing parasitic and input capacitance.

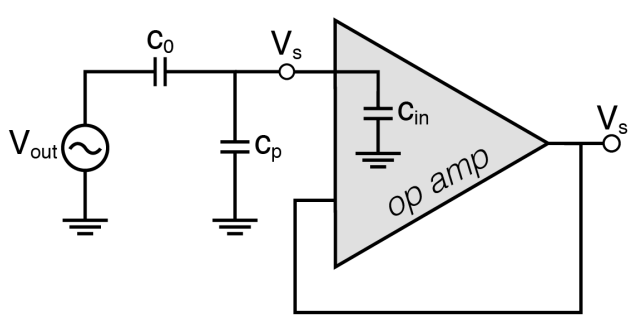

Figure 2.11: A schematic of the hydrophone output buffer circuit. C_0 is the clamped transducer capacitance, and C_p and C_{in} are the parasitic and op-amp input capacitances, respectively. The three capacitances create a potential divider, decreasing the measured voltage from the device.

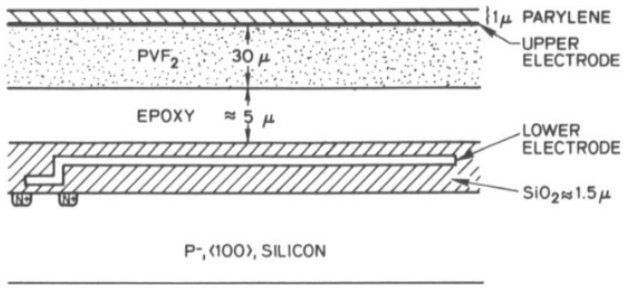

Figure 2.12: POSFET schematic [30]. This device minimizes the potential divider by having the transducer directly modulate the gate voltage of an on-chip FET.

Much research has gone into alleviating this issue, and one of the most effective methods of doing so is to integrate a piezoelectric transducer with an on-chip field effect transistor (FET) to form the so-called POSFET. The POSFET concept, which was originally developed by Swartz and Plummer [30] and is displayed in figure 2.12, allows the transducer to directly modulate the gate voltage on a FET, which has small input capacitance. The proximity to the FET also eliminates parasitics associated with the interconnects, but an additional capacitance is created between the lower electrode and the silicon substrate. This capacitance can be quite large because oxide growth is limited to a few microns in standard fabrication. The net impact of these effects is a decrease in the potential division, and the resulting POSFET performance has been thoroughly studied with finite element modeling [32] and experimental works [33].

This elegant solution is compatible with integrated-circuit fabrication, making it easily scalable to arrays with a large number of transducers and well-suited for mass production. For the researcher looking to explore new designs and transducer layouts, however, it is impractical. Outside of the mass production environment, transistor fabrication involves complex processing, several expensive photolithography masks, and specialized expertise. The resulting financial and practical burdens of prototyping POSFET arrays can effectively restrict creativity and innovation in PVDF acoustic transducers.

2.5 Conclusions and Design Alterations

PVDF has become one of the most highly utilized materials in underwater acoustic transducers, mainly because of its impedance match with water. Despite its lower piezoelectric coefficients and higher mechanical losses, its ability to exhibit quarter-wave resonance and its high transmission coefficient create a device with superior performance to conventional piezoelectrics. One significant drawback, however, is that PVDF has a low dielectric constant, meaning that as the transducer size is decreased in order to increase resolution, it becomes more difficult to obtain a useful voltage. The output signal must be buffered, but the transducer capacitance is sufficiently low that

the combined effect of parasitics and the input capacitance of op-amps will be debilitating on performance. Previous researchers have alleviated this problem by integrating on-chip transistors to create a POSFET, however, this poses a substantial manufacturing cost and is not conducive to prototyping, which was one of the main goals of this work.

With the previous issues in mind, some alterations to the proposed device are offered here. The electrodes will be patterned on the substrate to eliminate the contact pad capacitance, and the substrate will be an electrical insulator to further reduce parasitic capacitances. In aims of facilitating fabrication, the ground plane is also moved to the upper surface so that only one electrical connection to must be made to it. Candidate manufacturing methods for this are printed circuit boards or lift-off patterning on glass using simple microfabrication processes. The final device design including these alterations is shown in figure 2.13.

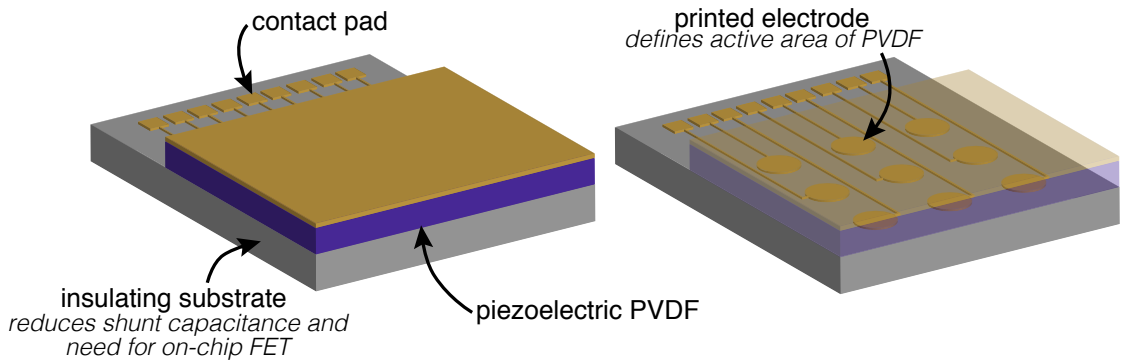

Figure 2.13: Updated device design. An insulating substrate is used to reduce parasitic capacitance that decreases device sensitivity. Defining electrodes on the substrate allows standard microfabrication methods to define the active transducer area, and contact pads away from the PVDF allow for connection to off-chip op-amps.

Chapter 3

Finite Element Modeling

Mathematical models are very powerful tools. They provide designers and engineers with simplified yet tractable analysis on which to base their intuition and fundamental understanding of a device. However, they are limited in several regards. Physical systems are typically governed by boundary conditions (BCs) and partial differential equations (PDEs), which oftentimes have obtainable solutions only when assumptions are made and complexities are omitted. For example, the analysis of a longitudinally vibrating transducer presented in Section 2.4 assumes that motion is restricted to one direction and is uniform across the device surface, and that in-plane stresses are negligible. While these are seemingly reasonable assumptions, no effort was made to explore the conditions that their validity is contingent on, or what impact they have.

Conversely, finite element modeling is gaining popularity as a way to include the full complexity of a system in its analysis and better predict the performance of devices. The finite element method (FEM) essentially breaks up a complex continuous geometry into many smaller elements, and approximately solves the governing PDEs over each element. With commercial FEM software packages, multiple physics (e.g. electrical and acoustical) may be coupled and solved simultaneously, and there are less restrictions on what may be analyzed. However, this can come at the cost of understanding; many times users of FEM software simply look into what is happening rather than *why* it is happening, which can have various detrimental repercussions. It is therefore desired to only use FEM when direct analysis will fail, but in order to do this, it must be known how and when the two methods will deviate. The goal of this chapter is to determine some of the conditions and implications of this disagreement while also developing models that will be of use to the design of acoustic transducers. This is done through the development of separate finite element models for hydrophones and projectors in COMSOL Multiphysics. The chapter concludes with the analysis of the electrical admittance of a PVDF projector; this is presented as an experiment that may be used in the future to verify the developed models.

3.1 Passive Imager: A One-Dimensional Hydrophone

In passive imaging systems such as the acoustic daylight concept presented in Chapter 1, the transducers need only act as hydrophones. Hydrophones are most sensitive to normally-incident waves (i.e., the wavefronts are parallel to the surface), thus the device performance in this case is a good metric by which to compare transducers. Furthermore, this case is relatively simple and readily compares with the theory developed in Section 2.4, which makes it a useful tool for gaining familiarity with FEM software.

3.1.1 Diffraction Effects

Analysis of hydrophones in the case of normally-incident acoustic waves is typically simplified, as is done in Chapter 2, to a one-dimensional problem. This approximation is not always valid, however, because a nonuniform pressure may develop across the surface of the transducer as a result of the transducer itself scattering acoustic energy. As shown in figure 3.1A, when the incident acoustic wave hits the surface, each point acts as a point-source of acoustic energy. P_A is therefore the sum of the incident pressure and the diffracted pressure from the rest of the device.

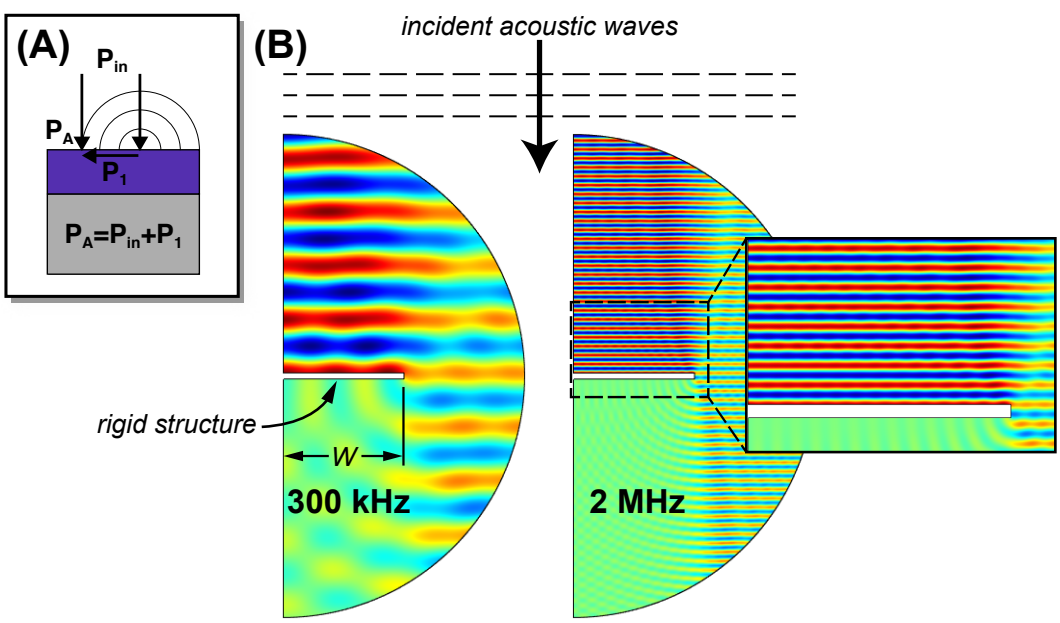

Figure 3.1: (A) Illustration of the cause of diffraction. P_A is the sum of the incident and reflected acoustic pressure from other points on the surface. (B) Simulated acoustic field near a rigid structure. When the wavelength is much smaller than the structure, plane waves are preserved and the acoustic pressure does not depend on position.

Exploration of this phenomenon can be done through a simple finite element model, as shown in figure 3.1B. The model applies a downward-moving $1\,\mu$Pa incident plane pressure wave along the semicircular periphery, and the acoustic field around a rigid boundary of $W = 1\,$cm is calculated (W corresponds to the size of the full device rather than that of an individual transducer). Each point on the transducer acts as a point source of scattered acoustic energy, and due to the relative phase variations of these scattered waves there is alternating constructive and destructive interference at different locations superimposed on the $1\,\mu$Pa incident plane wave. At higher frequencies (shorter wavelengths), however, there is sufficient symmetry that the reflected waves coherently form a plane wave of their own, thus the full acoustic field still consists of plane waves, aside from edge effects. Thus, when $W \gg \lambda$ the acoustic pressure doubles at the transducer-water interface (this is the reason for the factor of 2 in the Mason circuit pressure source in figure 2.6) but plane waves are preserved, so the one-dimensional assumption is valid.

3.1.2 Model setup

As mentioned previously, physical systems are defined by a combination of PDEs and BCs. For the sake of simplicity, COMSOL allows the user to specify a PDE by choosing from a set of preset physics interfaces; each physics interface automatically applies the correct governing PDE, and the user is left to choose proper BCs for their model. For the work presented in this report, all simulations are done in the frequency domain and used the preset "acoustic-piezoelectric interaction" interface, which links three physics: pressure acoustics, solid mechanics, and electrostatics. The governing PDEs of these three physics respectively are

$$-\nabla \cdot \frac{1}{\rho}(\nabla p - \mathbf{q}_d) - \frac{\omega^2}{\rho c^2} p = Q_m \tag{3.1}$$

$$-\rho\omega^2 \mathbf{u} - \nabla \cdot \mathbf{T} = \mathbf{F_v} e^{j\phi} \tag{3.2}$$

$$\nabla \cdot \mathbf{D} = \rho_e \tag{3.3}$$

Where in eq 3.1 Q_m is a monopole source term and $\mathbf{q}_d$ is a dipole source term. This equation is known as the inhomogeneous Helmholtz equation, and it is a three-dimensional extension of eq 2.5, written in terms of pressure rather than displacement. In eq 3.2, $\mathbf{T}$ is a 6×1 vector of stresses (in COMSOL this variable is σ), $\mathbf{u}$ is a 3×1 vector of displacements, and $\mathbf{F_v}$ is a volumetric body force term. In eq 3.3, $\mathbf{D}$ is electric displacement and ρ_e is the volumetric charge density. In all work presented in this report, Q_m, $\mathbf{q}_d$, and $\mathbf{F_v}$ are set to 0. The piezoelectric effect is implemented through a built-in multiphysics package that utilizes eq 2.15.

After selecting physics interfaces, the next steps in constructing a finite element model in COMSOL are defining the geometries, applying the BCs, and specifying materials. The geometry is laid out with boundary labels in figure 3.2. Boundary conditions were chosen to mimic the one-dimensional analysis and provide a voltage output; these are listed in table 3.1. Most BCs are intuitive, but a few require elaboration.

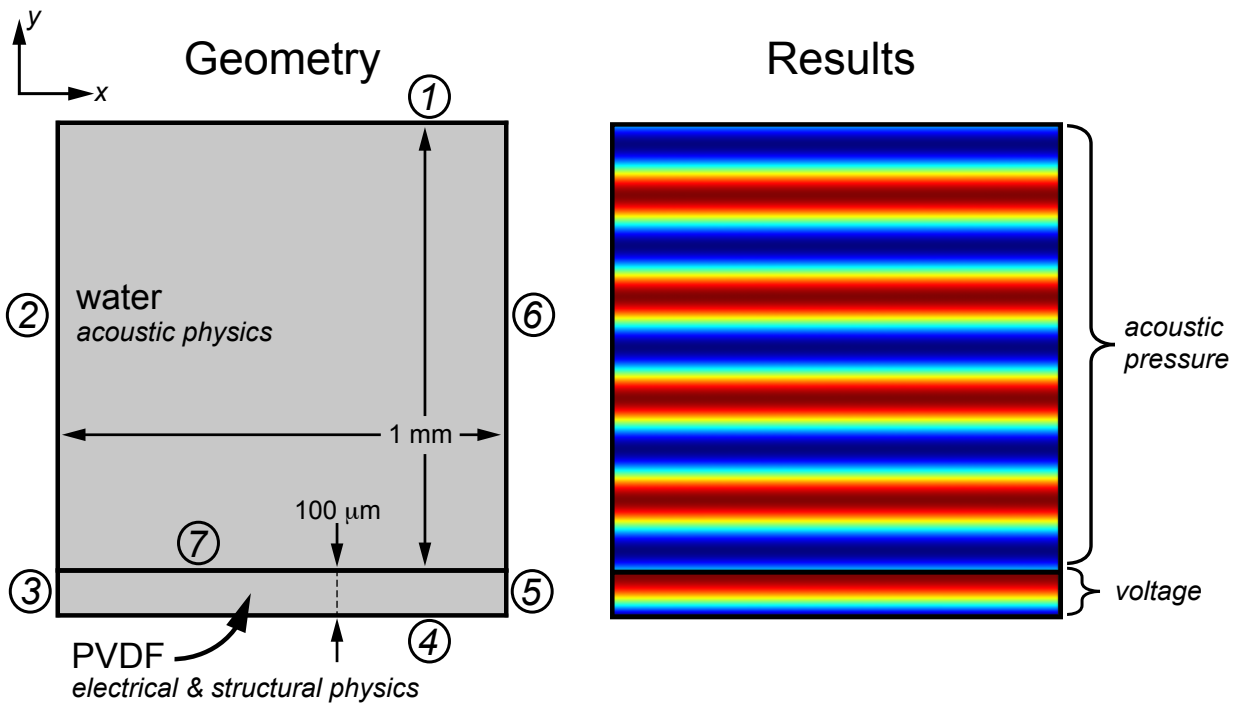

Figure 3.2: Left: Geometry and domains for the different physics used. Right: An illustration of typical results. Continuity BCs on 2 and 6 are used to suppress diffraction and ensure the existence of plane waves.

Table 3.1: Boundary conditions for simulations. Boundaries are labeled in figure 3.2

Boundary No.	Physics	Boundary Condition
1	acoustic	Plane wave radiation: $P_{in} = 1\,\mu\text{Pa}$
2 & 6	acoustic	Periodic continuity: eq 3.4
3 & 5	electrostatics	Zero charge: $\mathbf{n} \cdot \mathbf{D} = \varepsilon(\mathbf{n} \cdot \mathbf{E}) = 0$
3 & 5	solid mech.	Roller: $\mathbf{n} \cdot \mathbf{u} = 0$
4	solid mech.	Anchor: $\mathbf{u} = 0$
4	electrostatics	Ground: $V = 0$
7	electrostatics	Floating potential: $\int_S \mathbf{n} \cdot \mathbf{D} = 0$
7	multiphysics	Acoustic and structural continuity: eqs 3.5, 3.6

The incident acoustic field is simulated by applying a 1 µPa plane wave radiation along boundary 1. Note that this does not force the time-harmonic pressure amplitude along this border to be 1 µPa, as reflected waves may be superimposed. The acoustic periodic continuity BC (eq 3.4) is used to fulfill the condition for a valid one-dimensional approximation (i.e., $W \gg \lambda$). It specifies an equal and opposite pressure gradient along two opposing parallel boundaries, emulating an infinitely wide hydrophone by effectively making the simulation domain shown in figure 3.2 act as a "unit cell," where equal solutions would be present in cells to the left and right.

$$-\mathbf{n} \cdot \left(\frac{1}{\rho} (\nabla p - \mathbf{q_d}) \right) \bigg|_2 = \mathbf{n} \cdot \left(\frac{1}{\rho} (\nabla p - \mathbf{q_d}) \right) \bigg|_5 \tag{3.4}$$

where $\mathbf{n}$ is the outward facing normal vector of the respective boundary.

Stresses and displacements in the PVDF are solved using the solid mechanics physics, which must be coupled to the acoustic interface in the water to ensure a proper solution. The coupling is achieved by enforcing a continuity in pressure and acceleration along boundary 7:

$$\mathbf{n} \cdot \left(\frac{1}{\rho} (\nabla p - \mathbf{q_d}) \right) = \mathbf{n} \cdot \frac{\partial^2 \mathbf{u}}{\partial t^2} \tag{3.5}$$

$$\mathbf{F}_A = p\,\mathbf{n} \tag{3.6}$$

where $\mathbf{u}$ is the PVDF displacement, and $\mathbf{F_A}$ is the solid mechanics boundary load applied by the acoustic field.

After applying BCs, the materials must be defined in COMSOL. Per eq 3.1, the acoustic-domain material only requires definition of density and sound speed. The solid mechanics, electrostatics, and piezoelectric interfaces require specification of the constants in eq 2.15. PVDF is typically regarded as having isotropic elasticity and dielectric constants, so the following simplifications are used:

$$\begin{bmatrix} s_{11}^E & s_{12}^E & s_{13}^E & 0 & 0 & 0 \\ s_{21}^E & s_{22}^E & s_{23}^E & 0 & 0 & 0 \\ s_{31}^E & s_{32}^E & s_{33}^E & 0 & 0 & 0 \\ 0 & 0 & 0 & s_{44}^E & 0 & 0 \\ 0 & 0 & 0 & 0 & s_{55}^E & 0 \\ 0 & 0 & 0 & 0 & 0 & s_{66}^E \end{bmatrix} = \frac{1}{Y} \begin{bmatrix} 1 & -\nu & -\nu & 0 & 0 & 0 \\ -\nu & 1 & -\nu & 0 & 0 & 0 \\ -\nu & -\nu & 1 & 0 & 0 & 0 \\ 0 & 0 & 0 & 1+\nu & 0 & 0 \\ 0 & 0 & 0 & 0 & 1+\nu & 0 \\ 0 & 0 & 0 & 0 & 0 & 1+\nu \end{bmatrix} \tag{3.7}$$

$$\begin{bmatrix} \varepsilon_{11}^T & 0 & 0 \\ 0 & \varepsilon_{22}^T & 0 \\ 0 & 0 & \varepsilon_{33}^T \end{bmatrix} = \varepsilon_r \varepsilon_0 \mathbf{I_3} \tag{3.8}$$

where $\mathbf{I_3}$ is the identity matrix, Y is the Young's modulus, ν is the Poisson's ratio, ε_r is the relative permittivity of PVDF, and $\varepsilon_0 = 8.854 \times 10^{-12}$ F/m is the permittivity of free space. The value of all parameters used to define materials in COMSOL are listed in table 3.2. Water is a built-in material in COMSOL, but its values are included for reference.

For two-dimensional geometries, COMSOL solves the solid mechanics physics under the plane-strain assumption. In this case, the sound speed can be written as

$$c = \sqrt{\left(\frac{Y}{\rho}\right)\frac{1-\nu}{(1+\nu)(1-2\nu)}} \tag{3.9}$$

In the case of PVDF, this results in $c_{PVDF} = 1980$ m/s. The predicted quarter-wave resonance frequency of a 100 µm-thick PVDF transducer is therefore $f = c/4L$ =4.95 MHz.

The next and final step in the model setup is meshing. As a general rule, a minimum of 5-6 elements per wavelength are required to resolve wave propagation [34]. The shortest wavelength is dictated by water since it has a lower sound speed than PVDF, and to be safe a minimum of 10 elements per wavelength is chosen to simulate the hydrophone, as shown in figure 3.3. The mesh in all domains is a free triangular mesh with all parameters set at the default for the "fluid dynamics - finer" option, except the minimum element size is changed to

$$d_{min} = \frac{c_{water}}{10 f_{max}} \tag{3.10}$$

The resulting mesh with $f_{max} = 10$ MHz is displayed in figure 3.3. Simulations were also performed with $d_{min} = \lambda_{min}/8$ and $\lambda_{min}/15$ to ensure that the solution accuracy was insensitive to meshing at this point.

Table 3.2: Constants used to define PVDF and water in COMSOL

Material	Parameter	Value
PVDF [35]	Y	3 GPa
	ν	0.4
	ρ	1780 kg/m^3
	ε_r	10
	d_{31}	23×10^{-12} C/N
	d_{32}	2×10^{-12} C/N
	d_{33}	-33×10^{-12} C/N
	d_{24}, d_{15}	0 C/N
Water	ρ	999.62 kg/m^3
	c	1481.4 m/s

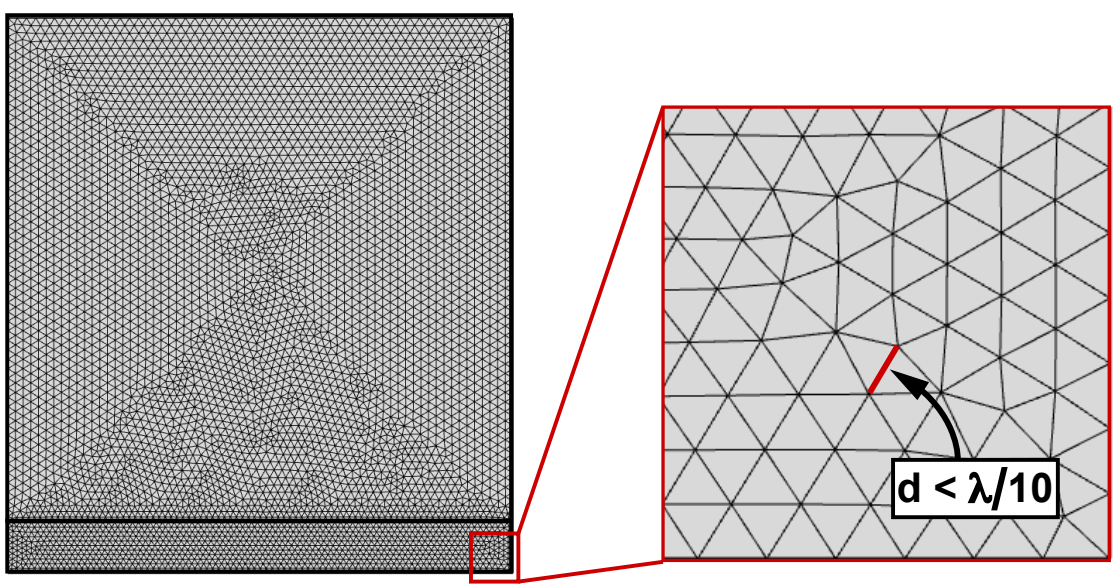

Figure 3.3: Mesh used for all hydrophone simulations. Element sizes are chosen such that there are at least 10 elements per wavelength at 10 MHz.

3.1.3 Open Circuit Voltage Sensitivity

One of the most important performance parameters of a hydrophone is its open circuit voltage sensitivity (OCVS), or the voltage output per unit pressure input when connected to an infinite-impedance electrical load. It may be conveniently calculated in COMSOL post-processing by dividing the potential at boundary 7 by 1 µPa, which was defined as the incident pressure amplitude. In order to capture the full 4.95 MHz quarter-wave resonance peak, COMSOL simulations are performed over a frequency range of 1-10 MHz. Note that the quarter-wave resonance corresponds to velocity resonance, but since voltage is proportional to strain and $v = j\omega u$, the OCVS resonance is slightly below 4.95 MHz.

The electrical output of the hydrophone can also be calculated using the methods presented in Section 2.4.1. With boundary 4 anchored, the substrate is treated as an infinite acoustic impedance and the Mason circuit simplifies as shown in figure 3.4A. The OCVS can then be derived as

$$\frac{V_{out}}{P_{in}} = \frac{2A_0 N}{j\omega C_0(\rho c_w A_0 + Z_a + Z_b)} \tag{3.11}$$

A comparison between the simulated and analytic voltage sensitivities is given in figure 3.4B, which shows a low-frequency sensitivity of 7.6×10^{-2} mV/Pa, more commonly written in equivalent form as -202 dB re 1V/µPa. This displays the impressive benefits of PVDF as a transduction material; this sensitivity is on par with typical Tonpilz PZT hydrophones. For example, the TC3027 acoustic transducer made by Teledyne Reson has a similar area and exhibits a peak sensitivity of -201 dB re 1V/µPa. Furthermore, this comparison displays a discrepancy of less than 1 part per thousand at all frequencies, which verifies the approach and boundary conditions used in the COMSOL modeling.

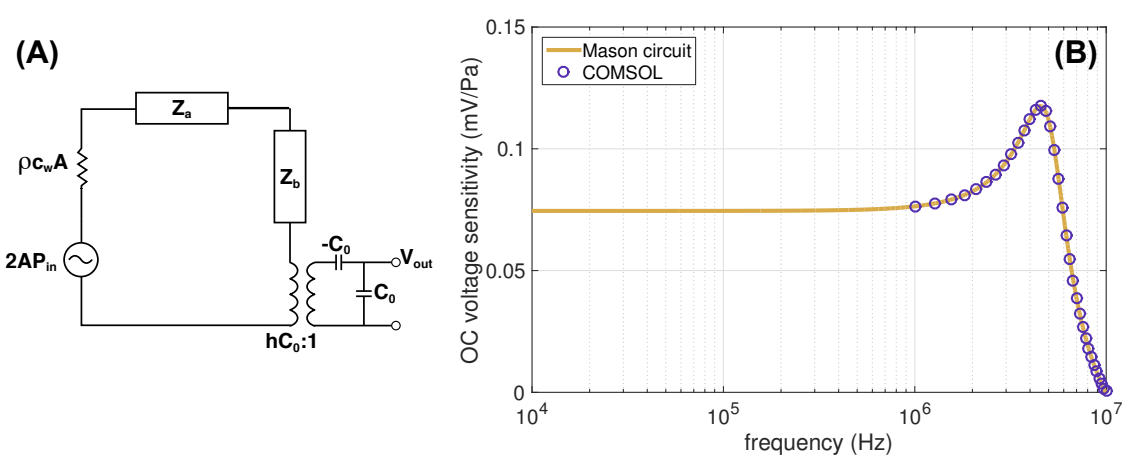

Figure 3.4: Comparison of modified Mason circuit (A) and COMSOL simulations (B). Results show a less than 1 part per thousand discrepancy at all frequencies.

3.2 Active Imager: An Axisymmetric Two-Dimensional Projector

Active imagers require both projectors and hydrophones, and it is preferable that the same transducers act as both (i.e., operate in pulse-echo mode). In order to explore the viability of the proposed design as a part of an active imaging system, the acoustic output must be calculated. Since the acoustic field is now being generated by the transducer, the effect of diffraction is determined by the ratio of transducer dimension to the acoustic wavelength, whereas in hydrophone operation the array dimension was critical. For this reason, diffraction is expected to play a larger role over a wider range of frequencies in projector operation, so significant care should be taken when invoking the one-dimensional approximation. The aim of this section is to evaluate the acoustic output from a single transducer, and to show how it compares to one-dimensional theoretic predictions.

3.2.1 Model setup

The projector model has many similarities with the hydrophone model developed in Section 3.1.2, however the fundamental approach of avoiding diffraction effects can no longer be taken. Luckily, the structure has a cylindrical symmetry that may reduce the complexity of the model, allowing utilization of the "2D Axisymmetric" interface in COMSOL. It is applicable because, due to the circular electrode pattern of the proposed transducer, the acoustic field is independent of angle about its center axis.

The geometry of the simulation domain is shown in figure 3.5, and the "acoustic-piezoelectric interaction" interface is again used. Eqs 3.5 and 3.6 are applied as before to the upper PVDF surface to couple the acoustic and structural physics. The bottom and right vertical PVDF boundary again have roller conditions as BCs for solid mechanics. The entire upper PVDF surface is set as electrical ground, and 1 V is applied only to the lower boundary of the active PVDF region. All other PVDF boundaries are set to a zero charge electrical BC. All edges that coincide with the symmetry axis are automatically prescribed axial symmetry conditions by COMSOL; these are left unchanged.

One major change must be made in the simulation of a projector, however: the addition of a perfectly matched layer (PML). Wave physics are particularly difficult to simulate with conventional FEM because there is no BC that simulates an infinite domain, and at any type of boundary there is some amount of reflection. PMLs effectively eliminate this problem by applying an exponential decay to waves passing through them [36]. This makes it so that the boundary condition on the outer edge of the PML *effectively does not matter*; any reflected wave from this boundary will return to the standard water domain exponentially tiny, and have no effect on simulation results.

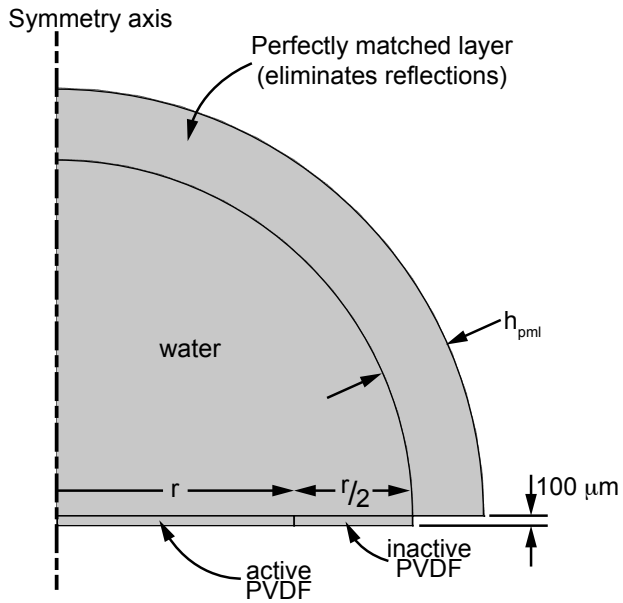

Figure 3.5: Geometry of simulation domain for the two-dimensional axisymmetric projector

PMLs are implemented in COMSOL simply by defining the physics (acoustics) and wave speed (c_w =1481 m/s) in the domain. In order to explore the effects of a changing geometry on the projector's performance, the active PVDF disk radius r is varied in the following simulations. The thickness is held constant at L =100 µm, and the PML thickness is set to h_{pml} =0.5 mm.

3.2.2 Transmitting Beam Pattern

As mentioned in Section 2.4.3, the transmitting beam pattern is determined by evaluation of the Rayleigh integral, eq 2.30. While a solution was obtainable for a uniformly vibrating transducer, this neglects the complexities of acoustic-structure interactions and is therefore not applicable in general. It is, however, of great interest to examine how the approximate case compares to reality in order to determine when one-dimensional analysis may be used, and what errors doing so may introduce.

Evaluation of the transmitting beam pattern is facilitated in COMSOL by the "far-field calculation" interface. This interface numerically computes the Rayleigh integral, eq 2.30, along a boundary in order to determine the radiated acoustic pressure. This function is defined in the Acoustics physics model section, and the boundary for evaluating the Rayleigh integral is chosen as the inner surface of the PML; this is far enough away from the radiating face that the small errors in the near-field finite element solution are not of significance.

Typical simulation results are illustrated in figure 3.6 for a transducer with $r = 2.5$ mm. As should be expected, the radiated acoustic field more closely resembles plane waves at high frequencies and the structural deformation is greatest at resonance. The effect of the inactive PVDF is also apparent; near the active-inactive PVDF junction there is a decrease in displacement due to the inactive material resisting motion of the active material. This decreases the acoustic output of the transducer as shown in figure 3.7, and has larger effects at high off-axis angles (i.e. $\theta = \pm 90°$). The radiated acoustic energy at these angles does not contribute to the intended function of the device, yet it does have significant impacts on the cross-talk between array elements. Since the MRA TVR is not degraded, the inactive PVDF actually gives a performance enhancement in this regard.

The transmitting beam pattern is studied by simulating devices with several different radii at 300 kHz, 1 MHz, and 3 MHz. Results from four illustrative cases are provided in figure 3.7, along with their corresponding one-dimensional approximation and a 3 dB error cone angle, which indicates the region within which the simulated and approximated solutions differ by less than 3 dB. There are two requirements for correctly invoking the one-dimensional approximation: the error cone angle must be large, and the TVR magnitude at the edge of the error cone must be much smaller than the MRA ($\theta = 0°$) magnitude. This will ensure that both methods correctly model a majority of the projector's radiated acoustic energy.

An excellent agreement between one-dimensional theory and full simulation is observed for the $r = 2.5$ mm projector. The error cones are large, and the TVR at the edge of the cone is at least 30 dB below the MRA TVR in all cases. Converseley, in the case of the $r = 100$ µm transducer, the TVR at the edge of the 3 dB error cone at 1 and 3 MHz is only about 2 and 8 dB below the MRA TVR, respectively. Even in the 1 MHz case, which has a wide error cone, this means that a substantial amount of the acoustic energy is *not* contained by the error cone, indicating that the two methods of analysis will not agree. At low frequencies (i.e. $r < \lambda$) the cause of the discrepancy is not the interference of acoustic waves, but rather the excitation of displacement modes other than the thickness-mode in the PVDF. A rule of thumb used in transducer design is that in order to suppress other modes it should be the case that $r/L \gg 1$, but no concrete number to this condition is suggested. The results here indicate that $r/L \approx 15$ is sufficient to isolate the thickness-mode.

The exact threshold for what constitutes a valid approximation depends on the specific system and application, but this analysis shows that the one-dimensional approximation can result in significant error depending on the transducer size. As transducer size decreases, it is increasingly important to utilize finite element modeling instead of one-dimensional analysis in order to correctly model the device performance.

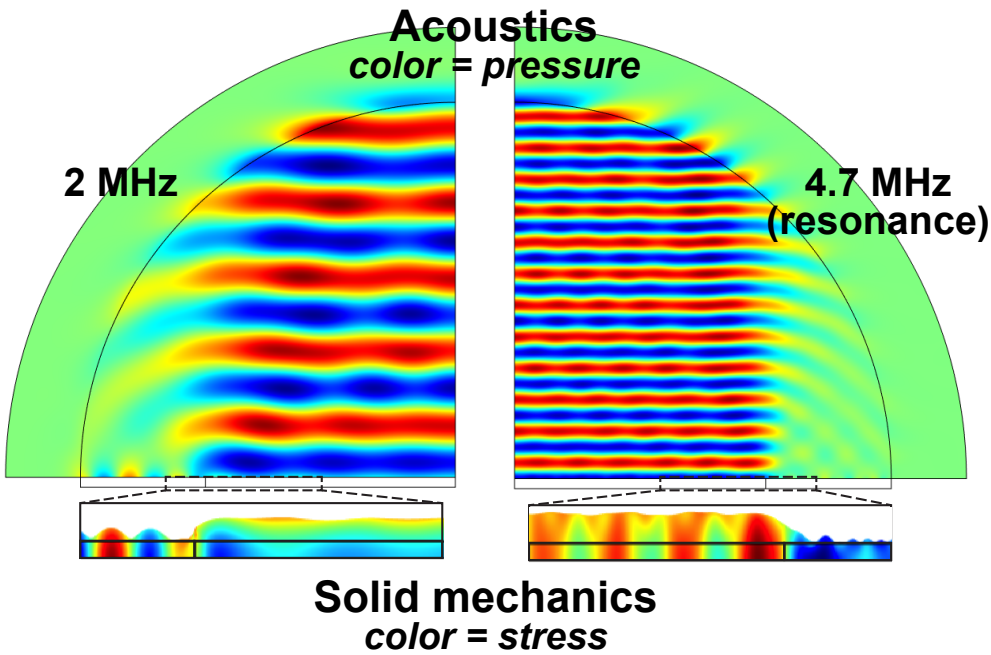

Figure 3.6: Visualization of results from projector simulations

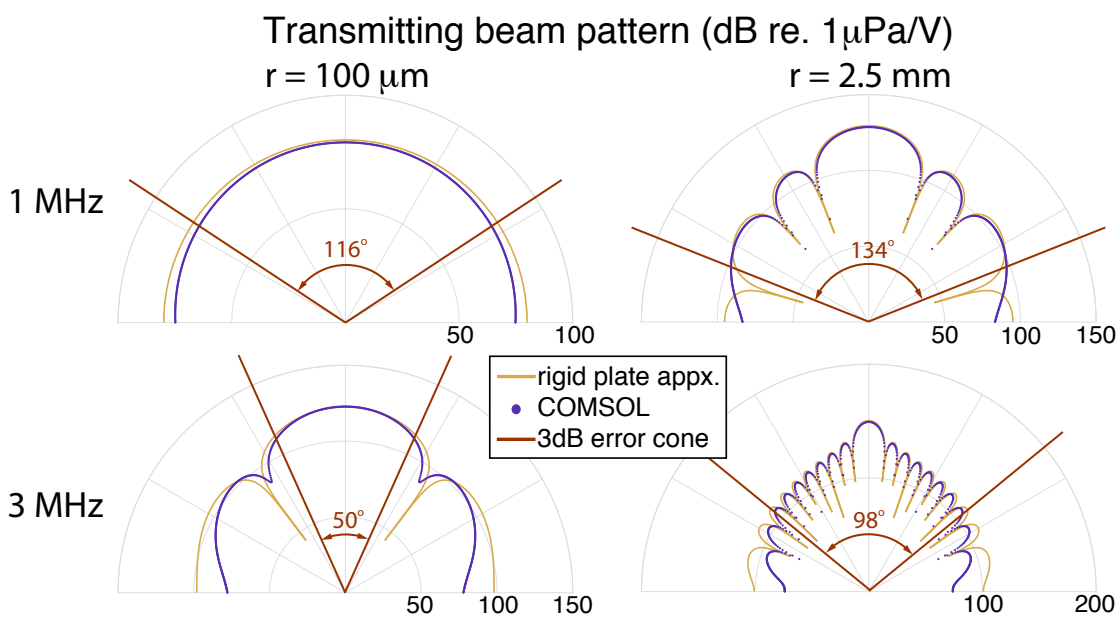

Figure 3.7: Transmitting beam patterns for different radius of active PVDF. The 3 dB error cone is defined as the cone within which the uniformly vibrating plate theory and COMSOL simulations differ by less than 3 dB.

3.2.3 Electrical Admittance

While finite element modeling is a useful tool in characterizing complex systems, it is of course only as good as the assumptions made in defining the system. These assumptions may include idealized BCs, treatment of electrical and mechanical losses, the omission of certain components, and so on. For this reason, it is absolutely crucial that a finite element model be verified to some extent before its use as a design tool. In the case of the acoustic transducer in this work, one very convenient way to verify the developed models is to measure the electrical admittance; this parameter is simple to measure and contains information of all the relevant system dynamics.

The electrical admittance is calculated in COMSOL in the post-processing step by taking the average current density over the lower boundary of active PVDF, multiplying by the active area of PVDF, and dividing by the applied voltage (1 V). The effect of device geometry on admittance is evaluated by performing a parametric sweep over r with $L = 100\,\mu\text{m}$, and each simulation covering a frequency range of 3.5-6 MHz. The results are shown in figure 3.8, with the percent error is defined as

$$\%\,\text{error} = \text{RMS}\Big(\frac{Y_{FEM}(f) - Y_{1D}(f)}{Y_{1D}(f)}\Big) \times 100 \tag{3.12}$$

where RMS is the vector root-mean-square operator, and subscript FEM and 1D denote the vector of admittances calculated in COMSOL and with the one-dimensional mason circuit, respectively. In figure 3.8 it can again be seen that larger transducers are approximated very well by the one-dimensional analysis, however even for the largest simulated geometry there is an undesired 5.5 MHz resonance mode present. This parasitic resonance is the reason that the error does not appear to tend towards 0 for large r/L. Nonetheless, based on these simulations it may be predicted that for transducers with $r/L > 17$, the measured electrical admittance will be within 5% of that predicted by the one-dimensional model.

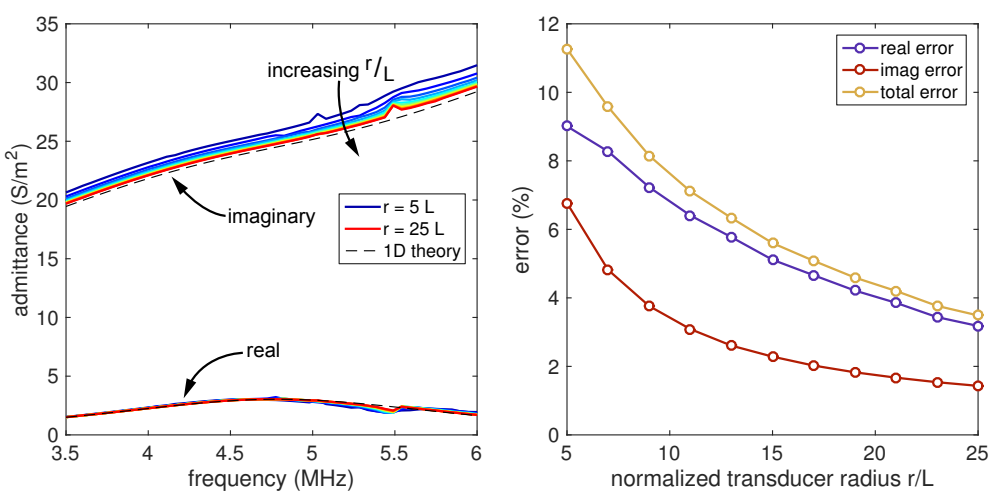

Figure 3.8: Results of electrical admittance simulations.

Chapter 4

Conclusions and Future Works

Acoustic imaging is one promising method of sensing in the ocean, but to be amenable to underwater wireless sensor networks (UWSNs), small and low-cost transducer arrays must be made. In aim of this, a PVDF acoustic imager is proposed and analyzed in this report. By nature of the piezoelectric material choice and use of standard microfabrication methods, the device is financially feasible and well-suited for both array fabrication and swarm implementation, as in UWSNs.

The performance of the proposed device was studied in-depth through direct and finite element analysis in COMSOL Multiphysics. This analysis revealed several benefits to using PVDF as a structural material in thickness-mode devices, such as a high bandwidth and sensitivity comparable to commercially available transducers. The analysis also had design implications, resulting in alterations to the original device architecture. Finally, the two analysis approaches were used to shed light on when the one-dimensional lumped-parameter approximation may be used, and what errors should be expected when invoking said approximation.

In the future, a prototype fabrication process will be developed and a test array of transducers with varying radius will be made. The transducers will be submerged in castor oil as shown in 4.1, and their frequency dependent electrical admittance will be measured using a network analyzer. Castor oil will be used because it is impedance-matched with water, and it eliminates problems associated with operating electronics in water. The results will be compared to the admittance calculated in COMSOL to validate the finite element models that were developed and presented in this report. Upon validation, these models will be a viable tool for the future design and analysis of thickness-mode PVDF transducers.

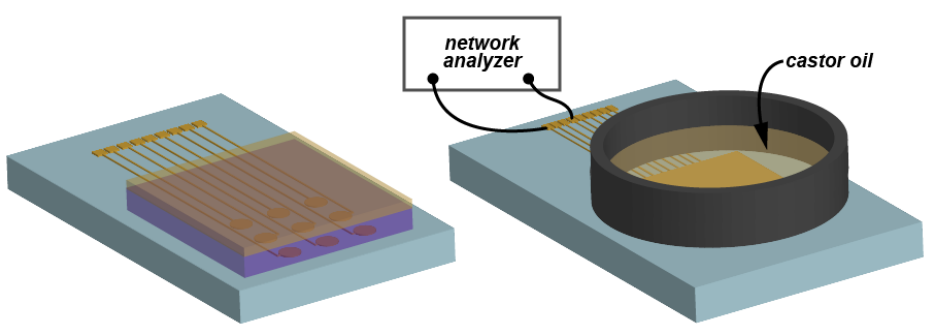

Figure 4.1: Future electrical admittance experimental setup.

Bibliography

[1] National Oceanic and Atmospheric Administration. *Ocean*. May 2015. URL: http://www.noaa.gov/ocean.html.

[2] National Oceanic and Atmospheric Administration. *Medicines from the Sea*. May 2015. URL: http://www.noaa.gov/features/economic_0309/medicines.html.

[3] K.E. Kohfeld et al. "Role of marine biology in glacial-interglacial CO2 cycles." In: *Science (New York, N.Y.)* 308.5718 (2005), pp. 74–78.

[4] B. Drogin. "Mapping an ocean of species". In: *Los Angeles Times* (Aug. 2009).

[5] R. Sandrea and I. Sandrea. "Deepwater Crude Oil Output: How Large Will the Uptick Be?" In: *Oil & Gas journal* 108.41 (2010).

[6] Jun-Hong Cui et al. "The challenges of building mobile underwater wireless networks for aquatic applications". In: *Network, IEEE* 20.3 (2006), pp. 12–18.

[7] Thomas B Curtin et al. "Autonomous oceanographic sampling networks". In: *Oceanography* 6.3 (1993), pp. 86–94.

[8] Prashant Kumar, P Priyadarshini, et al. "Underwater acoustic sensor network for early warning generation". In: *Oceans, 2012*. IEEE. 2012, pp. 1–6.

[9] Mari Carmen Domingo. "An overview of the internet of underwater things". In: *Journal of Network and Computer Applications* 35.6 (2012), pp. 1879–1890.

[10] Dorado-network.com. *Dorado-Network Sensor Network*. 2015. URL: http://www.dorado-network.com/v3/DN-SensorNetwork.html.

[11] G. Kokossalakis. "Acoustic Data Communication System for In-Pipe Wireless Sensor Networks". PhD thesis. Massachusetts Institute of Technology, 2006.

[12] Tae-Hee Won and Sung-Joon Park. "Design and implementation of an omni-directional underwater acoustic micro-modem based on a low-power micro-controller unit". In: *Sensors* 12.2 (2012), pp. 2309–2323.

[13] C. H. Sherman and J. L. Butler. *Transducer and arrays for underwater sound*. Springer, 2008.

[14] *Imaging in the ocean with ambient noise: the ORB experiments*. 1999. DOI: 10.1121/1.428175.

[15] Richard J Przybyla et al. "3D Ultrasonic Rangefinder on a Chip". In: (2015).

[16] KA Johannesson and RB Mitson. *Fisheries acoustics: a practical manual for aquatic biomass estimation*. Food and Agriculture Organization of the United Nations, 1983.

[17] Mohd Ikhwan Hadi Yaacob, Mohd Rizal Arshad, and Asrulnizam Abd Manaf. "Modeling and theoretical characterization of circular pMUT for immersion applications". In: *OCEANS 2010 IEEE-Sydney*. IEEE. 2010, pp. 1–4.

[18] Morten Wollert Nygren, Trond Ytterdal, and Tonni Franke Johansen. "Finite Element Modeling of Piezoelectric Ultrasonic Transducers". PhD thesis. 2011.

[19] S. W. Rienstra and A. Hirschberg. *An Introduction to Acoustics*. 2014.

[20] B. Jaffe, R.S. Roth, and S. Marzullo. *Properties of piezoelectric ceramics in the solid-solution series lead titanate-lead zirconate-lead oxide: Tin oxide and lead titanate-lead hafnate*. 1955. DOI: 10.6028/jres.055.028.

[21] Heiji Kawai. "The Piezoelectricity of Poly(vinylidene Fluoride)". In: *Japanese Journal of Applied Physics* 8 (1969), pp. 975–976. ISSN: 0021-4922. DOI: 10.1143/JJAP.8.975.

[22] L.F. Brown. "Ferroelectric polymers: current and future ultrasound applications". In: *IEEE 1992 Ultrasonics Symposium Proceedings* (1992). DOI: 10.1109/ULTSYM.1992.275948.

[23] AS Fiorillo et al. "A P(VDF-TrFE)-based integrated ultrasonic transducer". In: *Sensors and Actuators A: Physical* 22.1 (1990), pp. 719–725.

[24] QQ Zhang et al. "High frequency broadband PZT thick film ultrasonic transducers for medical imaging applications". In: *Ultrasonics* 44 (2006), e711–e715.

[25] Xinyu Li et al. "Pyroelectric and electrocaloric materials". In: *Journal of Materials Chemistry C* 1.1 (2013), pp. 23–37.

[26] F S Foster, K A Harasiewicz, and M D Sherar. "A history of medical and biological imaging with polyvinylidene fluoride (PVDF) transducers." In: *IEEE transactions on ultrasonics, ferroelectrics, and frequency control* 47.6 (2000), pp. 1363–1371. ISSN: 0885-3010. DOI: 10.1109/58.883525.

[27] V. Piefort. "Finite Element Modelling of Piezoelectric Active Structures". PhD thesis. Universite Libre de Bruxelles, 2000.

[28] Don Berlincourt. "Piezoelectric crystals and ceramics". In: *Ultrasonic transducer materials*. Springer, 1971, pp. 63–124.

[29] Yuan Yiquan, Shi Binwen, and Liu Zongjie. "New multilayer planar PVDF standard hydrophone and its applications". In: *IEEE Transactions on Ultrasonics, Ferroelectrics, and Frequency Control* 42.5 (1995), pp. 958–964. ISSN: 08853010. DOI: 10.1109/58.464848.

[30] R.G. Swartz and J.D. Plummer. "Integrated silicon-PVF¡inf¿2¡/inf¿acoustic transducer arrays". In: *IEEE Transactions on Electron Devices* 26.12 (1979). ISSN: 0018-9383. DOI: 10.1109/T-ED.1979.19797.

[31] John William Strutt Baron Rayleigh. *The theory of sound*. Vol. 2. Macmillan, 1896.

[32] G Uma et al. "Design and Simulation of PVDF-MOSFET Based MEMS Hydrophone". In: *Instrumentation Science and Technology* 35.3 (2007), pp. 329–339.

[33] Bei Zhu and Vijay K Varadan. "Integrated MOSFET-based hydrophone device for underwater applications". In: *SPIE's 9th Annual International Symposium on Smart Structures and Materials*. International Society for Optics and Photonics. 2002, pp. 101–110.

[34] Lorenzo Spicci and Marco Cati. "Ultrasound Piezodisk Transducer Model for Material Parameter Optimization". In: Comsol Conference. 2010.

[35] Measurement Specialties. "Piezo Film Sensors Technical Manual". In: *Measurement* March (2006), p. 57. URL: `www.msiusa.com`.

[36] Steven G Johnson. "Notes on perfectly matched layers (PMLs)". In: *Lecture notes, Massachusetts Institute of Technology, Massachusetts* (2008).